# Cavity quantum electrodynamics with a single molecule: Purcell enhancement, strong coupling and single-photon nonlinearity

**Daqing Wang**

Max-Planck Institute for the Science of Light, Staudtstr. 2, 91058 Erlangen, Germany

*Present address:* Institute of Physics, University of Kassel, Heinrich-Plett-Str. 40, 34132 Kassel, Germany

E-mail: `daqing.wang@uni-kassel.de`

March 2021

**Abstract.** Control of light-matter coupling at the quantum level is an enabling technique for many emerging quantum technologies. This tutorial describes recent advances in achieving efficient coupling of light with a single molecule using an optical Fabry-Perot microcavity. We demonstrate that the efficient cavity-molecule coupling converts the molecule to an effective two-level system. In this regime, a single molecule can act as a nearly perfect reflecting mirror and exhibits optical nonlinearity at the ultimate level of single photons.

## 1. Introduction

In the past century, understanding and controlling of light-matter interaction have triggered enormous advances in science and technology. Developments of lasers, semiconductor light emitting devices and imaging sensors, have reshaped our modern society. The upcoming 'second quantum revolution' [1], where new quantum technologies based on manipulating single quantum systems and utilizing unique quantum phenomena, such as superposition and entanglement, promises fast computation, secure communication and metrology with unprecedented precision [2]. In the blueprint of a 'quantum internet' [3, 4], quantum information will be processed and stored at distributed nodes in atomic qubits. Inter-connectivity will be realized by single photons serving as quantum information carriers. Realizing such a vision requires the control of light-matter interaction at its ultimate level of single photons and single atoms.

An elementary example is the interaction of a single photon with a single two-level atom – the picture we have learned in our physics education: a photon flies in, an atom is excited. Although this picture is so fundamental and intuitive, to make a single photon interact deterministically with a single atom remains a challenging experimental task. Despite the simplicity of such a system, coupling photons efficiently to a single two-level atom can demonstrate rather striking effects, such as the reversal of spontaneous emission [5, 6], perfect light refection from a two-level atom [7] and optical nonlinearity at the single-photon level [8–10].

In this tutorial, we introduce our recent work on achieving efficient coupling of light to a single atom-like quantum system. Our choice of 'atoms' are polycyclic aromatic hydrocarbon (PAH) molecules embedded in solid-state matrices [11]. PAHs are photon emitters with remarkable optical properties, such as near-unity quantum efficiency, long-term photostability, and lifetime-limited transitions when cooled to liquid helium temperatures. Being embedded in solid state materials, they are compatible with optical microscopy techniques, using which light can be confined to a diffraction-limited spot around a single molecule. However, like other emitters in the solid state [12, 13], the electronic transitions in a PAH molecule couple to its internal vibrations and the solid-state environment that surrounds it [11]. As a result, the coherent 0-0 zero-phonon lines (00ZPL) transition has a branching ratio of about $30\% \sim 50\%$, limiting the coherent interaction efficiency with a light field. To overcome the decoherence induced by the vibronic coupling, we use an optical microcavity [14] to selectively enhance the 00ZPL transition via the Purcell effect [15]. We show that the 00ZPL transition can be enhanced

by a factor of 40 to dominate over the incoherent transitions, thus converting the molecule to a coherent two-level system. The strong Purcell-enhancement also reshapes the emission pattern of the molecule, enabling a near-unity coupling efficiency with the cavity mode. As a result of this efficient coupling, the system exhibits optical nonlinearity at the single-photon level [16].
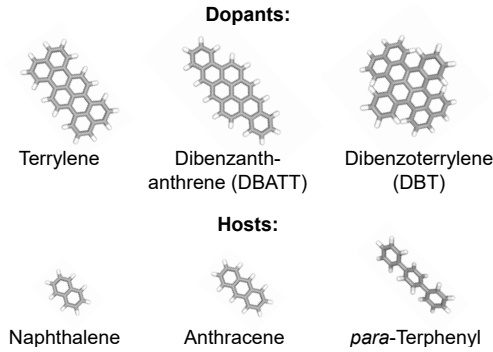
This tutorial is structured as follows. In section 2, we introduce the photophysics of PAH molecules embedded in solid-state materials. We review the fundamentals of cavity quantum electrodynamics (cavity QED) in section 3 and present the theoretical model for molecule-cavity coupling in section 4. After introducing the experimental platform in section 5, we discuss the observations of coherent molecule-cavity coupling in section 6. The nonlinear response of the system is described in section 7. Furthermore, we present an experiment where two molecule are interconnected using single photons in section 8. At the end, we draw a conclusion and outline future prospectives in section 9 †.

## 2. PAH molecules in a solid-state matrix

PAH molecules are composed of multiple fused aromatic rings, resembling cut-out pieces of a graphene sheet. The cyclic conjugated $\pi$-electrons in the molecule can be excited via an optical transition with transition frequencies ranging from ultraviolet to near infrared, depending on the structure and size of the molecule [18]. Since the late 1980s, a number of experiments have shown that PAH molecules can behave favorably as single quantum emitters when embedded in organic matrices and cooled to liquid helium temperatures ($T \leqslant 4.2\,\mathrm{K}$) [11]. Examples of commonly used PAH molecules for single-molecule studies are shown in the upper row of Fig. 1. The molecules are normally doped into an organic matrix with a larger optical band gap (see lower row in Fig. 1), such that the dopants act as optically active defect centers with a small concentration and can be detected via high-resolution microscopy and spectroscopy [11]. The first optical detection of single molecules was reported in 1989, where pentacene molecules embedded in *para*-terphenyl crystal were detected using frequency-modulation spectroscopy [19]. This pioneering work was recognized by the Nobel Prize in Chemistry in 2014.

When embedded in a matrix, the molecules take a fixed orientation and their rotational degrees of freedom freeze out. The energy levels of a PAH molecule

---

†This tutorial is based on a dissertation [17] that was awarded the 2020 SAMOP dissertation prize of the German Physical Society (DPG). Some text and figures are reproduced from the dissertation.

**Dopants:**

Terrylene  Dibenzanth-  Dibenzoterrylene
anthrene (DBATT)  (DBT)

**Hosts:**

Naphthalene  Anthracene  *para*-Terphenyl

**Figure 1.** Examples of commonly used PAH molecules (upper row) and hosting matrices (lower row) in single-molecule optical studies.

thus involve electronic and vibrational structures. As illustrated in Fig. 2 (a), the electronic ground state $|S_0\rangle$ of a PAH molecule is a singlet state, where the two electrons in the highest occupied molecular orbital are paired to give a total spin of zero. An electron in $|S_0\rangle$ can be excited to the lowest singlet excited state $|S_1\rangle$ via an optical transition (green arrow). A molecule also possesses a large number of vibrational modes, which couple to the electronic states and give rise to vibrational sub-levels. When excited to a higher vibrational level of the electronic excited state $|S_1, v \neq 0\rangle$, it quickly relaxes non-radiatively to the lowest vibrational level $|S_1, v = 0\rangle$, following Kasha's rule [20]. From $|S_1, v = 0\rangle$, the molecule can decay to the $|S_0, v = 0\rangle$ or $|S_0, v \neq 0\rangle$ levels by emitting a photon. The photon emission process is called fluorescence and the probabilities of decaying to each of the ground-state sub-levels follow the Franck-Condon principle [21, 22]. The optical transition connecting the $|S_1, v = 0\rangle$ and $|S_0, v = m\rangle$ levels is referred to as the 0-$m$ zero-phonon-line (ZPL) with $m = (0, 1, 2, ...)$. In particular, we denote the $|S_0, v = 0\rangle$ to $|S_1, v = 0\rangle$ transition as 00ZPL. Being surrounded by the solid-state matrix, the optical transitions are also coupled to the phononic modes of the lattice, giving rise to phonon wings associated with each of the ZPLs. Figure 2 (b) illustrates the emission spectrum from the $|S_1, v = 0\rangle$ state. The ZPLs appear as sharp peaks each accompanied by a broad phonon wing. Figure 2 (c) displays a measured emission spectrum from the $|S_1, v = 0\rangle$ state of a dibenzoterrylene (DBT) molecule embedded in an anthracene crystal and cooled to 4 K. The sharp peak at 784 nm corresponds to the 00ZPL transition. The Stokes-shifted ZPLs and the phonon wings are displayed in black.

A coefficient which we will come across often in this tutorial is the branching ratio of the 00ZPL emission $\alpha$, which is defined as the decay rate from $|S_1, v = 0\rangle$ to $|S_0, v = 0\rangle$ normalized to the total decay rate from
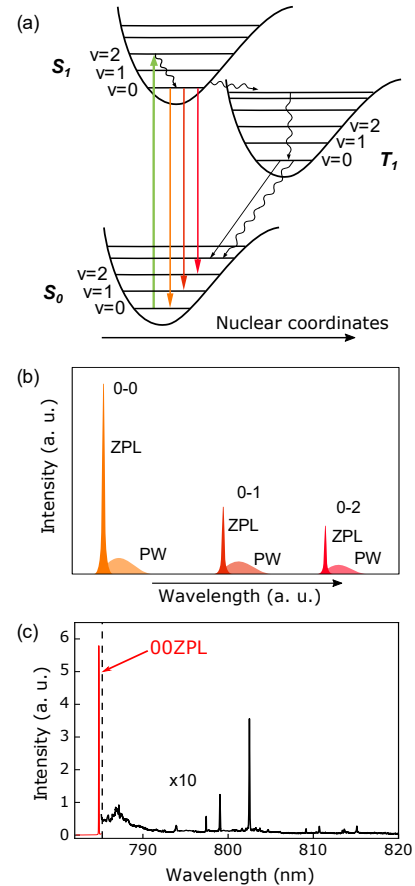
**Figure 2.** (a), Energy level structures of a PAH molecule embedded in a matrix. $S_0$: singlet ground state; $S_1$: low-lying singlet excited state; $T_1$: low-lying triplet excited state. The vibrational sub-levels are indicated by $v = 0, 1, 2$. The straight arrows denote optical transitions, while the curly arrows stand for non-radiative relaxations. (b), Emission spectrum from the $|S_1, v = 0\rangle$ state consists of zero-phonon lines and phonon wings. (c), Emission spectrum of a Dibenzoterrylene molecule in an anthracene crystal measured at 4 Kelvin.

$|S_1, v = 0\rangle$:

$$\alpha = \frac{\gamma_{\mathrm{zpl}}}{\gamma^0}, \tag{1}$$

where $\gamma_{\mathrm{zpl}}$ and $\gamma^0$ denote the 00ZPL and total decay rates of $|S_1, v = 0\rangle$, respectively.

The transition between $|S_0\rangle$ and $|S_1\rangle$ is spin conserving. When an electron is excited to the singlet excited states, there is also a possibility that it undergoes a spin conversion and reaches a triplet state $|T_1\rangle$ (see Fig. 2 (a)), where the electrons are unpaired and give a total spin of one. This process is called intersystem crossing (ISC) and normally results from spin-orbit coupling [18]. From $|T_1\rangle$, the molecule can decay to $|S_0\rangle$ via another ISC process or by emitting a photon. The emission from $|T_1\rangle$ to $|S_0\rangle$ is called phosphorescence. We note that the ISC rate is molecule and host-matrix dependent. For systems such

as DBT molecules in anthracene crystals, the ISC yield can be as low as $10^{-7}$ [23].

When addressing the $|S_0, v = 0\rangle$ to $|S_1, v = 0\rangle$ transition using a narrow-linewidth laser, the fast relaxations of the $|S_0, v \neq 0\rangle$ levels and a negligible ISC rate allow efficient cycling of electrons back to the $|S_0, v = 0\rangle$ level. Thus, the molecule can be approximated as a two-level system. As shown in the following sections, the incoherent decays to the $|S_0, v \neq 0\rangle$ levels can be considered as an additional loss channel in the formulation of cavity quantum electrodynamics.

## 3. An introduction to cavity quantum electrodynamics

The radiative rate of a quantum emitter is not a constant, but rather depends on its surrounding electromagnetic environment. In free space, the excited state of a single emitter couples to vacuum fields of an infinite number of modes, giving rise to spontaneous emission with a rate described by the Einstein $A$ coefficient [24, 25]. The situation is different when the emitter is placed in an optical cavity. The frequency selectivity of the cavity allows only a discrete set of electromagnetic modes and modifies the radiative property of the emitter inside [26, 27]. In this section, we introduce the theoretical foundations of cavity quantum electrodynamics (cavity QED), which describes the interaction of a quantum emitter with a single cavity mode.

### 3.1. The Purcell factor

The first known reference to a cavity QED effect is the formulation by Edward M. Purcell in 1946 on the modification of spontaneous emission rates by a resonant circuit [15]. In his short paragraph in a conference proceeding, Purcell predicted that the nuclear magnetic transitions at radio frequencies could be enhanced via resonant coupling to an electrical circuit, by a factor of

$$F = \frac{3\lambda^3}{4\pi^2} \cdot \frac{Q}{V},$$ (2)

where $\lambda$ is the transition wavelength. $Q$ and $V$ are the quality factor and the volume of the electrical circuit, respectively. The enhancement factor $F$ is hence named the Purcell factor.

A simple but yet instructive derivation of the Purcell factor can be obtained using Fermi's golden rule. We follow the derivations in Ref. [28], consider a two-level emitter with a ground state $|g\rangle$ and an excited state $|e\rangle$ separated by $\hbar\omega_0$ in energy. The spontaneous emission rate $\gamma$ of the emitter can be calculated using Fermi's golden rule

$$\gamma = \frac{2\pi}{\hbar^2} |M_{eg}|^2 \rho(\omega_0),$$ (3)

where $M_{eg}$ is the transition matrix element and $\rho(\omega_0)$ is the density of states (DOS) of photons at the location of the emitter‡. In free space, the photonic density of states $\rho^0(\omega)$ as a function of frequency $\omega$ is giving by

$$\rho^0(\omega) = \frac{\omega^2 V_0}{\pi^2 c^3},$$ (4)

where $c$ is the speed of light in vacuum and $V_0$ is a volume applied for field quantization. The transition matrix element can be expressed as

$$M_{eg} = \langle -\boldsymbol{\mu_{eg}} \cdot \boldsymbol{E}_{\text{vac}} \rangle,$$ (5)

where $\boldsymbol{\mu_{eg}}$ is the dipole moment of the transition with amplitude $\mu_{eg} = -e \cdot \langle g|x|e \rangle$. $\mathbf{E}_{\text{vac}}$ denotes the electric field of the vacuum modes [29] with amplitude

$$E_{\text{vac}} = \left( \frac{\hbar\omega}{2\epsilon_0 V_0} \right)^{1/2},$$ (6)

with $\epsilon_0$ the vacuum electric permittivity. Since vacuum fields in free space have no preferential polarization, a factor of $1/3$ needs to be included to account for the random orientation of the field with respect to the transition dipole. The expression of $|M_{eg}|^2$ becomes:

$$|M_{eg}|^2 = \frac{\mu_{eg}^2 \hbar\omega}{6\epsilon_0 V_0}.$$ (7)

Combining Eqs. 3, 4 and 7, we obtain the spontaneous emission rate in free space

$$\gamma^0 = \frac{\mu_{eg}^2 \omega_0^3}{3\pi\epsilon_0 \hbar c^3}.$$ (8)

We now consider a two-level emitter placed in the field maximum of a cavity. Assuming the cavity has only one resonance mode close to the transition frequency of the emitter, the DOS of the cavity mode seen by the emitter is

$$\rho'(\omega_0) = \frac{\kappa/(2\pi)}{(\omega_0 - \omega_c)^2 + (\kappa/2)^2},$$ (9)

which is a normalized Lorentzian function with center frequency $\omega_c$ and full width at half maximum (FWHM) $\kappa$. In the expression of $E_{\text{vac}}$ (see Eq. 6), the mode volume $V_0$ should be replaced by the mode volume of

---

‡The initial and final states consist of both the states of the emitter and the photon. Since the final state of the electron is defined to be the ground state $|g\rangle$, after integrating over all the possible final states, only the photonic DOS is present.
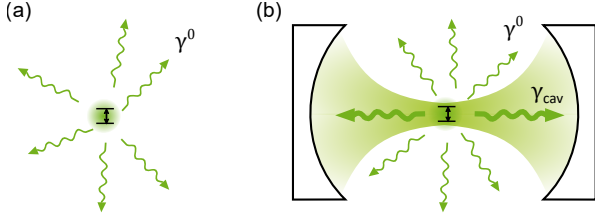
**Figure 3.** (a), A two-level system with spontaneous emission rate of $\gamma^0$ in free space. The direction of emission is random. (b), When resonantly coupled to a cavity, the spontaneous emission is enhanced by an amount of $\gamma_{\text{cav}}$. The emission rate into free-space modes can be considered unchanged.

the cavity $V$. For a cavity in vacuum, the mode volume can be calculated as

$$V = \frac{\int_{V_{\text{cav}}} \epsilon_0 |\mathbf{E}(\mathbf{r})|^2 \mathrm{d}^3 \mathbf{r}}{\max[\epsilon_0 |\mathbf{E}(\mathbf{r})|^2]}, \qquad (10)$$

where $\mathbf{E}(\mathbf{r})$ stands for the electric field at point $\mathbf{r}$ in the volume of the cavity $V_{\text{cav}}$. We also note that the electric field in the cavity can hold a defined polarization and aligned to the emitter, meaning that the factor of $1/3$ can be omitted in the expression of $|M_{eg}|^2$. The modified spontaneous emission rate into the cavity mode $\gamma_{\text{cav}}$ is then

$$\gamma_{\text{cav}} = \frac{2\mu_{eg}^2 Q}{\hbar \epsilon_0 V} \cdot \frac{(\kappa/2)^2}{(\omega_0 - \omega_c)^2 + (\kappa/2)^2}, \qquad (11)$$

where we have used $Q = \omega/\kappa$. Considering that the cavity only affects the DOS within its finite solid angle, one can assume the emission rate into free-space modes unmodified (see Fig. 3). The total emission rate of the emitter in the cavity $\gamma'$ can be expressed as

$$\gamma' = \gamma_{\text{cav}} + \gamma^0. \qquad (12)$$

The ratio of the cavity-modified emission rate to the free-space rate is

$$\frac{\gamma_{\text{cav}}}{\gamma^0} = \frac{3\lambda^3}{4\pi^2} \cdot \frac{Q}{V} \cdot \frac{(\kappa/2)^2}{(\omega_0 - \omega_c)^2 + (\kappa/2)^2}. \qquad (13)$$

When the frequency of the cavity is tuned on resonance with the emitter, Eq. 13 simplifies to the form of the Purcell factor given in Eq. 2:

$$F = \frac{3\lambda^3}{4\pi^2} \cdot \frac{Q}{V}. \qquad (14)$$

We note that for the simplicity of the derivation, we have only considered an emitter in vacuum. A factor of $1/n^3$ is thus missing in Eq. 14 compared to the more common form of the Purcell factor [28]. In fact,

the treatment of spontaneous emission enhancement for an emitter embedded in a dielectric or plasmonic structure is often complicated, where the expression of $V$ in Eq. 10 requires revision. A self-consistent electromagnetic theory which provides the explicit form of $V$ and correctly recovers the expression of $F$ is presented in Ref. [30].

A useful coefficient which describes the efficiency of emission into a particular mode is the $\beta$-factor, defined as the ratio of the power emitted into the single mode to the total emitted power [31]. The $\beta$-factor of emission into the cavity mode can be written as

$$\beta = \frac{\gamma_{\text{cav}}}{\gamma'} = \frac{F}{F+1}. \qquad (15)$$

The figure of merit of a cavity for spontaneous emission enhancement is given by $Q/V$, namely the ratio of its quality factor over its mode volume. It is, thus, desirable to fabricate cavities with a high $Q$ and a small $V$ to achieve a large spontaneous emission enhancement [14].

### 3.2. The Jaynes-Cummings Hamiltonian

Having worked through the Purcell factor, we now introduce the Hamiltonian formulation of a coupled emitter-cavity system. At the end of this section, we will comment on the equivalence of the DOS and the Hamiltonian approach in describing the Purcell effect.

The total Hamiltonian of a coupled emitter-cavity system can be written as

$$H = H_{\text{e}} + H_{\text{c}} + H_{\text{int}}, \qquad (16)$$

where $H_{\text{e}} = \hbar\omega_0(\sigma_+\sigma_- - \sigma_-\sigma_+)/2$ represents the Hamiltonian of the emitter with $\sigma_+ = |e\rangle\langle g|$ and $\sigma_- = |g\rangle\langle e|$ the atomic raising and lowering operators satisfying the anti-commutation relation $\{\sigma_-, \sigma_+\} = \mathbb{1}$. The Hamiltonian of the cavity mode is denoted by $H_{\text{c}} = \hbar\omega_c a^\dagger a$, in which $a^\dagger$ and $a$ stand for its creation and annihilation operators§. The Hamiltonian $H_{\text{int}}$ describes the interaction between the emitter and the cavity. Considering only the electric dipolar interaction, $H_{\text{int}}$ takes the form

$$H_{\text{int}} = -\boldsymbol{\mu_{eg}} \cdot \mathbf{E}_{\text{vac}}. \qquad (17)$$

Assuming that the transition dipole of the emitter is aligned with the polarization of the cavity field and adapting the formulations in Ref. [27], $H_{\text{int}}$ can be written as

$$H_{\text{int}} = -\mu_{eg}(\sigma_- + \sigma_+) \cdot iE_{\text{vac}}(a - a^\dagger). \qquad (18)$$

§We set the vacuum energy $\hbar\omega_c/2$ as the zero of the energy in the cavity mode. The zero of the emitter's energy is set at the middle of $|e\rangle$ and $|g\rangle$.

Here, $E_{\text{vac}}$ stands for the amplitude of vacuum electric field in the cavity. After expanding the scalar product, the terms containing $\sigma_- a$ and $\sigma_+ a^\dagger$ can be negated using the rotating-wave approximation. The interaction Hamiltonian simplifies to

$$H_{\text{int}} = -i\hbar g(\sigma_+ a - \sigma_- a^\dagger) \tag{19}$$

with

$$g = \left(\frac{\mu_{eg}^2 \omega_c}{2\hbar\epsilon_0 V}\right)^{1/2} \tag{20}$$

the emitter-cavity coupling strength (or the vacuum Rabi frequency). We restrict our further analysis to the first excited states of the system, i.e. the system has one excitation with two possible excited states of $|e,0\rangle$ and $|g,1\rangle$. Here, the letter in the ket represents the state of the emitter and the digit denotes the number of photons in the cavity mode. The Hamiltonian can be expressed by a $2 \times 2$ matrix:

$$H = \hbar \begin{bmatrix} \omega_0 & -ig \\ ig & \omega_c \end{bmatrix} - \frac{1}{2}\hbar\omega_0 \mathbb{1}. \tag{21}$$

After diagonalizing $H$, we obtain the two eigenenergies of the excited states

$$E_\pm = \hbar\left[\frac{\omega_c}{2} \pm \sqrt{\left(\frac{\omega_0 - \omega_c}{2}\right)^2 + g^2}\right], \tag{22}$$

and the two corresponding eigenstates

$$\begin{aligned}|+\rangle &= \cos\theta\,|e,0\rangle + i\sin\theta\,|g,1\rangle\ , \\ |-\rangle &= \sin\theta\,|e,0\rangle - i\cos\theta\,|g,1\rangle\ ,\end{aligned} \tag{23}$$

with

$$\tan 2\theta = \frac{2g}{\omega_0 - \omega_c}. \tag{24}$$

One notices that the two excited states of the system $(|+\rangle, |-\rangle)$ are both entangled states of the emitter and the cavity mode. In Fig. 4(a), we plot the two eigenenergies $(E_+, E_-)$ as functions of the frequency detuning between the emitter and the cavity. The two eigenenergies show clear avoided crossing and the amount of splitting at zero detuning equals $2\hbar g$. This splitting is often called vacuum Rabi splitting [32].

### 3.3. Quasi-eigenstate coalescence and strong coupling

So far, we have considered a system without dissipation. A realistic system always interacts with its environment. For example, the emitter can radiate into free-space modes and the cavity field can leak via its mirrors. In the density matrix formalism, a non-Hermitian Hamiltonian can be used to account for dissipation. We follow Ref. [33] and express the non-Hermitian Hamiltonian as

$$H' = H - i\hbar\gamma^0(\sigma_+\sigma_- - \sigma_-\sigma_+)/2 - i\hbar\kappa a^\dagger a/2 \tag{25}$$

with $H$ the Hermitian Hamiltonian defined in Eq. 16 and $\kappa$, $\gamma^0$ the dissipation rates of the cavity field and the emitter into free space, respectively. $H'$ can also be expressed in the matrix formulation:

$$H' = \hbar \begin{bmatrix} \omega_0 - i\gamma^0/2 & -ig \\ ig & \omega_c - i\kappa/2 \end{bmatrix} - \frac{1}{2}\hbar\omega_0 \mathbb{1}. \tag{26}$$

After diagonalizing $H'$, we obtain the quasi-eigenenergies of the system:

$$\begin{aligned}E'_\pm(\omega_0 - \omega_c) = &\hbar\frac{\omega_c - i(\gamma^0 + \kappa)/2}{2} \\ &\pm \hbar\sqrt{\left(\frac{\omega_0 - \omega_c + i(\kappa - \gamma^0)/2}{2}\right)^2 + g^2}.\end{aligned} \tag{27}$$

The imaginary parts of the quasi-eigenenergies translate to the half widths of the spectral lineshape. When the cavity and the emitter are resonantly coupled ($\omega_c = \omega_0$), the quasi-eigenenergies simplify to

$$E'_\pm(0) = \hbar\left[\frac{\omega_0}{2} - \frac{i(\gamma^0 + \kappa)}{4} \pm \sqrt{g^2 - \left(\frac{\kappa - \gamma^0}{4}\right)^2}\right]. \tag{28}$$

When $g < |\kappa - \gamma^0|/4$, the term in the square root is negative and the real part of $E'_\pm(0)$ can only take the value of $\hbar\omega_0/2$. In the case of $g > |\kappa - \gamma^0|/4$, the real part of $E'_\pm(0)$ can take two different values, representing the energies of two quasi-eigenstates. The point where $g = |\kappa - \gamma^0|/4$ is thus referred to as the exceptional point (EP) [33].

Fig. 4(b) and (c) display the real and imaginary parts of $E'_\pm(0)$ as a function of $g$ (normalized to $|\kappa - \gamma^0|$), respectively. The location of the EP is marked by the green dots. In the limit of $g \gg |\kappa - \gamma^0|/4$, the two quasi-eigenenergies approach the values in the non-dissipative case given in Eq. 22. The splitting of the eigenenergies is normally a sign of entering the strong-coupling regime of cavity QED. More often, this regime is considered to be reached when a system satisfies $g \gg (\kappa, \gamma^0)$ [34]. In this regime, the rate of resonant energy exchange between the emitter and the cavity mode is higher than the dissipation rates of the system [27], meaning that the emitter and the cavity can exchange a quantum of excitation for a certain number of rounds within the irreversible dissipation time.

When $g$ is smaller than one of the dissipation rates ($g < \kappa$ or $g < \gamma^0$), the system is in the weak-coupling
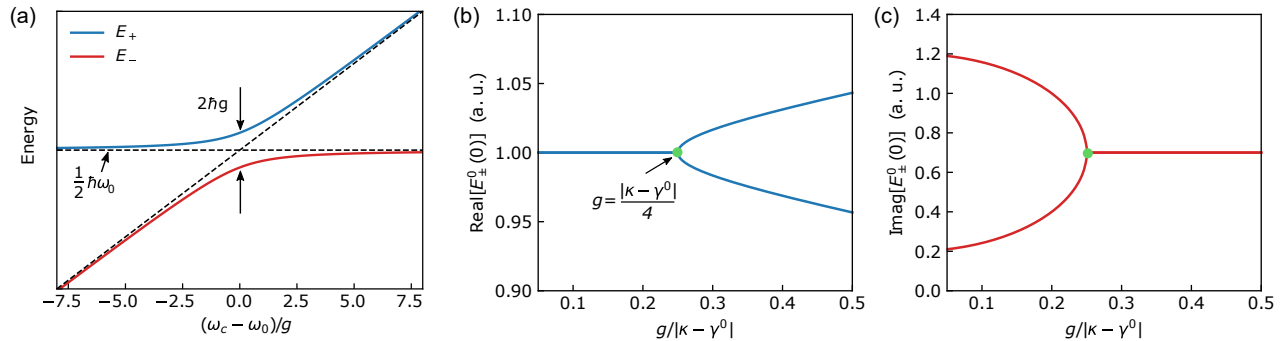
**Figure 4.** (a), Dependence of the two eigenenergies $E_+$ (blue line) and $E_-$ (red line) on the emitter-cavity frequency detuning. The amount of splitting at zero detuning equals $2\hbar g$. Energies of uncoupled emitter and cavity are shown by the dashed lines. (b) Real and (c) imaginary parts of $E'_\pm(0)$ as a function of $g$. The green dots mark the location of the exceptional point. $(\kappa, \gamma^0)/2\pi = (1.2, 0.2)$ GHz are used in this example.

regime. In this regime, the coherent energy exchange between the emitter and the cavity mode is slower than the dissipation of the system. Nevertheless, for an emitter with a linewidth narrower than that of the cavity ($\gamma^0 < \kappa$), its radiative property is still influenced by the Purcell effect.

When the dissipation rate of the cavity is much larger than the other two rates ($\kappa \gg 2g$ and $\kappa \gg \gamma^0$), the two quasi-eigenenergies in Eq. 28 can be approximated to

$$E'_+(0) = \frac{1}{2}\hbar\omega_0 - i\hbar\left(\frac{\gamma^0}{2} + \frac{2g^2}{\kappa}\right),$$

$$E'_-(0) = \frac{1}{2}\hbar\omega_0 - i\hbar\left(\frac{\kappa}{2} - \frac{2g^2}{\kappa}\right). \tag{29}$$

The first eigenvalue $E'_+(0)$ represents the energy of the emitter, while the second ($E'_-(0)$) represents that of the cavity mode [34]. The imaginary part of $E'_+(0)/\hbar$ corresponds to the half width of the emitter resonance and hence reveals the decay rate of the emitter in the cavity:

$$\gamma' = \gamma^0 + \frac{4g^2}{\kappa}. \tag{30}$$

The term $4g^2/\kappa$ stands for the net enhanced emission rate into the cavity mode. The same quantity is denoted by $\gamma_{\mathrm{cav}} = F \cdot \gamma^0$ in section 3.1. Combining Eqs. 11, 14 and 20, one can identify that

$$F \cdot \gamma^0 = 4g^2/\kappa. \tag{31}$$

The Hamiltonian and the DOS treatments are thus consistent in describing the Purcell effect in the weak-coupling regime.

Next, we introduce another important parameter in cavity QED, namely the cooperativity $C$, defined as

$$C = \frac{\gamma_{\mathrm{cav}}}{\gamma^0} = \frac{4g^2}{\kappa\gamma^0}. \tag{32}$$

We note that for an ideal two-level emitter, $F$ and $C$ are identical. However, $F$ is more commonly used for weakly coupled systems, whereas $C$ appears often in the discussions of the strong-coupling regime.

## 4. Interaction of a molecule with a cavity mode

We now focus on the scenario of a single molecule coupled to a cavity. Following Ref. [35], we derive the complex transmission and reflection coefficients of the coupled system. First, we work in the weak-excitation regime and study the modifications to the molecular linewidth and center frequency. The phase shift on an incident laser beam is also discussed. We then study the nonlinear response of the system at increasing pump powers. Lastly, we derive the photon statistics of the light transmitted through the system.

### 4.1. Transmission and reflection spectra

The molecule can be approximately treated as a two-level system (TLS) given the fast relaxations of the $|S_0, v \neq 0\rangle$ levels. The decays from $|S_1, v = 0\rangle$ into these levels are accounted for by including an additional dissipation rate $\gamma_{\mathrm{red}}$ to the upper level. We denote the free-space spontaneous emission rate of a molecule as $\gamma^0$, which equals the sum of the emission rates via the 00ZPL ($\gamma_{\mathrm{zpl}}$) and $\gamma_{\mathrm{red}}$. The non-radiative decay and pure dephasing are not considered, since both rates are negligible for PAH molecules at liquid helium temperatures [11, 36].
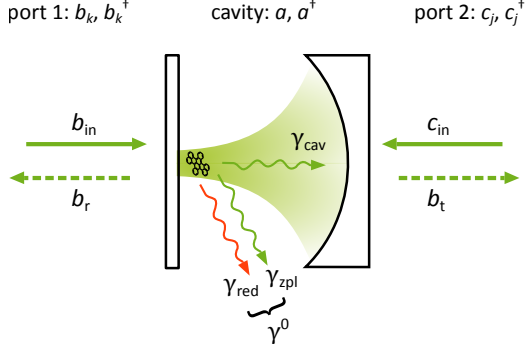
**Figure 5.** Illustration of a molecule coupled to a single-mode cavity. Spontaneous emission rate of the molecule in free space is denoted by $\gamma^0$, which equals the sum of $\gamma_{\mathrm{zpl}}$ and $\gamma_{\mathrm{red}}$. $\gamma_{\mathrm{cav}}$ stands for the net enhanced emission rate by the cavity. The cavity mode is represented by the annihilation operator $a$ and couples to the free space modes in port 1 and port 2 via its two mirrors. The fields in port 1 and port 2 are represented by the annihilation operators $b_k$ and $c_j$, respectively. $b_{\mathrm{in}}$ and $c_{\mathrm{in}}$ denote the input fields from port 1 and 2, $b_r$ and $b_t$ represent the reflected and transmitted fields of the incident field $b_{\mathrm{in}}$.

As depicted in Fig. 5, the molecule is placed in a cavity consisting of two mirrors. The cavity's resonance frequency $\omega_c$ is tuned to match the 00ZPL frequency of the molecule $\omega_0$. The narrow linewidth of the cavity resonance allows selective coupling to only the 00ZPL transition and keeping all the red-shifted decay channels off-resonant. The coupling enhances the 00ZPL transition by $\gamma_{\mathrm{cav}} = F \cdot \gamma_{\mathrm{zpl}}$, where $F$ is the Purcell factor. Since the cavity mirrors only cover a finite solid angle (up to $1.3\pi$ in our experiments), we assume that the spontaneous emission rate of the molecule to all other modes is unmodified. The total decay rate of the molecule in the cavity can thus be written as $\gamma' = \gamma_{\mathrm{cav}} + \gamma^0$.

We use $|g\rangle$ and $|e\rangle$ to denote $|S_0, v = 0\rangle$ and $|S_1, v = 0\rangle$ states and the corresponding atomic raising and lowering operators are written as $\sigma_+ = |e\rangle\langle g|$ and $\sigma_- = |g\rangle\langle e|$. We consider a symmetric cavity, where the two mirrors are non-absorptive and have equal transmission coefficients. The photon creation and annihilation operators of the cavity mode are denoted by $a^\dagger$ and $a$. The cavity mode is coupled to the electromagnetic modes in free space (port 1, port 2) via its two mirrors (see Fig. 5). The photon annihilation (creation) operators of port 1 and 2 are denoted as $b_k$ ($b_k^\dagger$) and $c_j$ ($c_j^\dagger$), respectively. The following derivations are based on Ref. [35] and adapted to the system under study.

The Hamiltonian of the coupled molecule-cavity system can be written as

$$
\begin{aligned}
H =& \hbar\omega_0(\sigma_+\sigma_- - \sigma_-\sigma_+)/2 + \hbar\omega_c a^\dagger a \\
& - i\hbar g(\sigma_+ a - \sigma_- a^\dagger) + \sum_k \hbar\omega_k b_k^\dagger b_k + \sum_j \hbar\omega_j c_j^\dagger c_j \\
& - i\hbar \sum_k (g_1 b_k^\dagger a - g_1 a^\dagger b_k) - i\hbar \sum_j (g_2 c_j^\dagger a - g_2 a^\dagger c_j),
\end{aligned}
$$
$$(33)$$

where $\omega_k$ ($\omega_j$) denotes the frequency of the field in port 1 (2), $g$ represents the molecule-cavity coupling strength defined in Eq. 20, $g_1$ and $g_2$ are real constants standing for the coupling strengths of the cavity mode to the modes in port 1 and 2, respectively.

In the next step, we write down the Heisenberg equation of motion (EOM) for the operators using

$$
\frac{dO(t)}{dt} = \frac{i}{\hbar}[H, O(t)] + \left(\frac{\partial O(t)}{\partial t}\right)_H \tag{34}
$$

with $O(t)$ a time-dependent operator, to arrive at

$$
\begin{aligned}
\dot{\sigma}_- &= -i\omega_0 \sigma_- + g\sigma_z a, \\
\dot{\sigma}_z &= -2g(\sigma_+ a + a^\dagger \sigma_-), \\
\dot{b}_k &= -i\omega_k b_k - g_1 a, \\
\dot{c}_j &= -i\omega_l c_j - g_2 a, \\
\dot{a} &= -i\omega_c a + g\sigma_- + g_1 \sum_k b_k + g_2 \sum_l c_j, \tag{35}
\end{aligned}
$$

where $\sigma_z = \sigma_+\sigma_- - \sigma_-\sigma_+$.

We use the operators $b_{\mathrm{in}}$ and $c_{\mathrm{in}}$ to represent the input fields from port 1 and port 2. The transmitted field $b_t$ and the reflected field $b_r$ (with respect to $b_{\mathrm{in}}$, the incident field from port 1) are defined as following

$$
\begin{aligned}
b_r &= b_{\mathrm{in}} - \sqrt{\frac{\kappa}{2}} a, \\
b_t &= c_{\mathrm{in}} - \sqrt{\frac{\kappa}{2}} a, \tag{36}
\end{aligned}
$$

where $\kappa$ denotes the decay rate of the cavity field, corresponding to the FWHM of the cavity's transmission spectrum. We note that despite the damping, the fluctuations of $b_r$ and $b_t$ maintain the commutator relations of $a$. The quantities $b_{\mathrm{in}}^\dagger b_{\mathrm{in}}$, $c_{\mathrm{in}}^\dagger c_{\mathrm{in}}$, $b_r^\dagger b_r$ and $b_t^\dagger b_t$ carry the unit of number of photons per unit of time, representing the power in their respective channel.

Combining Eqs. 35, 36, the temporal evolution of $a$ becomes

$$
\dot{a} = -i\omega_c a - \frac{\kappa}{2} a + g\sigma_- + \sqrt{\frac{\kappa}{2}}(b_{\mathrm{in}} + c_{\mathrm{in}}). \tag{37}
$$
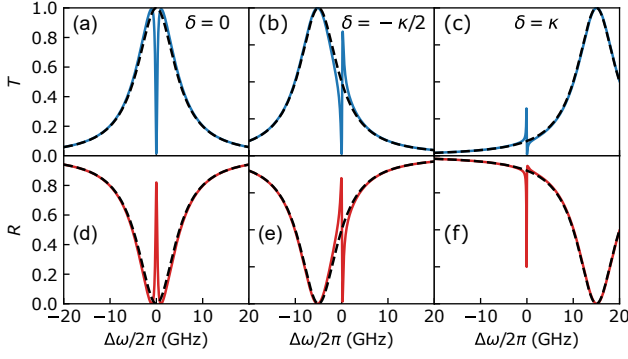
**Figure 6.** Transmission and reflection spectra of the coupled molecule-cavity system. (a), (b), (c), Blue curves display the transmission spectra with $\delta = (0, -\kappa/2, \kappa)$, respectively. The reflection spectra are shown by the red lines in (d), (e), (f). Dashed black lines represent the transmission spectra of the empty cavity. $(\kappa, \gamma^0, \gamma_{\text{cav}})/2\pi = (10, 0.04, 0.4)$ GHz are used for this example.

We express the EOMs in the rotating frame at the laser frequency $\omega_l$, to arrive at

$$\dot{\sigma}_- = i\Delta\omega\sigma_- + g\sigma_z a,$$
$$\dot{\sigma}_z = -2g(\sigma_+ a + a^\dagger \sigma_-),$$
$$\dot{a} = i(\Delta\omega - \delta)a - \frac{\kappa}{2}a + g\sigma_- + \sqrt{\frac{\kappa}{2}}(b_{\text{in}} + c_{\text{in}}), \quad (38)$$

with $\Delta\omega = \omega_l - \omega_0$ and $\delta = \omega_c - \omega_0$¶. The coupling of the molecule with the free-space modes can be taken into account by adding the spontaneous emission rate $\gamma^0$ into the EOMs [35], which become

$$\dot{\sigma}_- = i\Delta\omega\sigma_- + g\sigma_z a - \frac{\gamma^0}{2}\sigma_-,$$
$$\dot{\sigma}_z = -2g(\sigma_+ a + a^\dagger \sigma_-) - \gamma^0(\sigma_z + 1),$$
$$\dot{a} = i(\Delta\omega - \delta)a - \frac{\kappa}{2}a + g\sigma_- + \sqrt{\frac{\kappa}{2}}(b_{\text{in}} + c_{\text{in}}). \quad (39)$$

In the weak excitation limit, the population of the excited state is negligible, i.e. $\langle\sigma_z\rangle \approx -1$. Hence, we can neglect the correlation between the cavity field and the excited state population, implying $\langle\sigma_z a\rangle = \langle\sigma_z\rangle\langle a\rangle$. When considering a steady-state response, we set $\dot{a} = 0$ and obtain

$$a = \frac{g\sigma_- + \sqrt{\kappa}(b_{\text{in}} + c_{\text{in}})}{-i(\Delta\omega - \delta) + \kappa/2} . \quad (40)$$

In an experiment, light are normally coupled into the cavity from only one port. In the following, we consider light incidence from port 1 ($c_{\text{in}} = 0$) and use $b_{\text{in}}$, $b_r$,

¶We note the differences in the conventions of $\kappa$ and $\Delta\omega$ in Ref. [35] and this tutorial. $\kappa$ and $\Delta\omega$ quoted in this tutorial correspond to $2\kappa$ and $-\Delta\omega$ in Ref. [35].

$b_t$ to represent their corresponding mean values. After inserting Eq. 40 into the EOMs, we arrive at

$$\dot{s} = i\Delta\omega s - \frac{\gamma_{\text{cav}}}{2}\left(t_0 + \frac{\gamma^0}{\gamma_{\text{cav}}}\right)s + \sqrt{\frac{\gamma_{\text{cav}}}{2}}b_{\text{in}}t_0,$$

$$b_t = -t_0 b_{\text{in}} + \sqrt{\frac{\gamma_{\text{cav}}}{2}}t_0 s,$$

$$b_r = b_{\text{in}} + b_t , \quad (41)$$

where $s = \langle\sigma_-\rangle$ and

$$t_0 = \frac{-1}{1 - i\dfrac{\Delta\omega - \delta}{\kappa/2}} \quad (42)$$

denotes the transmission coefficient of an empty cavity. The transmission coefficient of the coupled molecule-cavity system can be obtained by taking the ratio of the transmitted field $b_t$ to the incident field $b_{\text{in}}$:

$$t = \frac{b_t}{b_{\text{in}}}$$
$$= t_0 \cdot \left[1 - \frac{1}{1 + \left(i\dfrac{2\Delta\omega}{\gamma_{\text{cav}}} - \dfrac{\gamma^0}{\gamma_{\text{cav}}}\right)\left(i\dfrac{\Delta\omega - \delta}{\kappa/2} - 1\right)}\right] . \quad (43)$$

Similarly, the complex reflection coefficient $r$ can be calculated with

$$r = \frac{b_r}{b_{\text{in}}} = 1 + t . \quad (44)$$

In an experiment, one normally measures the transmission and reflection coefficients in energy $(T, R)$, which are related to the complex coefficients $t$, $r$ by

$$T = |t|^2 ,$$
$$R = |r|^2 . \quad (45)$$

The blue curves in Fig. 6 (a)-(c) represent exemplary transmission spectra of a coupled system calculated with $(\kappa, \gamma^0, \gamma_{\text{cav}})/2\pi = (10, 0.04, 0.4)$ GHz and for three different molecule-cavity detunings. The transmission spectra without coupling to the molecule (empty cavity) are plotted as the dashed black lines. The resonant coupling to the molecule introduces a dip in the transmission spectrum (see (a)), which is a result of destructive interference of the molecular scattering with the cavity field [35]. When the cavity is detuned from the molecular resonance (see (b), (c)), the interference shows up as a Fano-shaped signal [37], since the phase of the molecular scattering flips sign from the red to the blue side of its resonance. The red curves in Fig. 6 (d)-(f) present the reflection spectra of the system with the same parameters as in (a)-(c).

When the cavity is tuned on resonance (as shown in (d)), the molecule introduces a peak in the reflection signal, which confirms that the interaction is a coherent interference effect rather than purely absorptive.

Using Eqs. 43-45, we can calculate the amplitude of the resonant ($\delta = 0, \Delta\omega = 0$) transmission and reflection of the coupled system:

$$T_{\mathrm{res}} = (1 - \beta)^2 \,,$$
$$R_{\mathrm{res}} = \beta^2 \,, \tag{46}$$

where $\beta = \gamma_{\mathrm{cav}}/(\gamma_{\mathrm{cav}} + \gamma^0)$ is the $\beta$-factor of emission into the cavity mode. One would intuitively expect a stronger coherent interaction when the molecule scatters more efficiently into the cavity mode. As evidenced by Eq. 46, in the limit of $\beta = 1$, the molecule acts as a perfect mirror: it blocks the transmission completely ($T_{\mathrm{res}} = 0$) and reflects all the incident light back to the input port ($R_{\mathrm{res}} = 1$).

### 4.2. Purcell effect and Lamb shift

It is well known that the modification of the photonic density of states affects the linewidth and the center frequency of an atom [27, 38]. The former effect is known as the Purcell effect [15], discussed at the beginning of this section. The latter effect can be considered a modification to the Lamb shift [29, 39], which results from the coupling of the electronic transition to vacuum fields. Here, we show that both effects depend on the molecule-cavity detuning and can be extracted from the transmission spectrum.

We denote the linewidth of the molecular resonance and the change in its center frequency $\gamma$ and $\delta\omega_0$, respectively. Starting from Eq. 43 and Eq. 45, we consider a regime in which the cavity resonance is much broader than the modified molecular resonance ($\kappa \gg \gamma^0, \kappa \gg \gamma_{\mathrm{cav}}$). In the vicinity of the molecular frequency ($|\Delta\omega| \lesssim \gamma_{\mathrm{cav}}/2$), we can make the approximation $\Delta\omega/\kappa \approx 0$ and simplify the expression of $T$ to the product of the empty-cavity transmission $T_{\mathrm{cav}} = |t_0|^2$ and a generalized Lorentzian function, i.e. the sum of a dissipative and a dispersive Lorentzian profile with the same center frequencies and linewidths. The linewidth and center frequency of the generalized Lorentzian profile are given by

$$\gamma(\delta) = \left( \frac{\kappa^2}{4\delta^2 + \kappa^2} \cdot F + 1 \right) \cdot \gamma^0 \,,$$
$$\delta\omega_0(\delta) = -\frac{\delta\kappa F}{4\delta^2 + \kappa^2} \cdot \gamma^0 \,. \tag{47}$$

The solid blue curve in Fig. 7 (a) displays the transmission spectrum of a system with $(\kappa, \gamma^0, \gamma_{\mathrm{cav}}, \delta)/2\pi = (10, 0.04, 0.4, -5)$ GHz according to Eqs. 43 and 45.
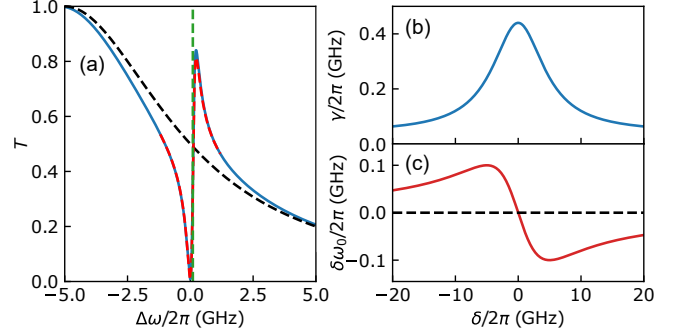


**Figure 7.** (a), Blue line displays the transmission spectrum of the coupled system calculated using $(\kappa, \gamma^0, \gamma_{\mathrm{cav}}, \delta)/2\pi = (10, 0.04, 0.4, -5)$ GHz. The dashed black line shows the spectrum of an empty cavity. The red line represents the calculated spectrum in the vicinity of the molecule using a generalized Lorentzian function. The vertical green line marks the center frequency of the generalized Lorentzian function. (b), (c), Linewidth and frequency shift of the molecule as a function of the molecule-cavity detuning, respectively. The dashed black line in (c) marks the frequency of the molecule in free space.

The dashed red line shows the spectrum calculated using the generalized Lorentzian profile. The close agreement between the two curves confirms the validity of the approximation. The dashed black line represents the spectrum of an empty cavity.

The molecular linewidth $\gamma$ is a Lorentzian function of $\delta$. When the cavity is tuned on resonance with the molecule, $\gamma = \gamma_{\mathrm{cav}} + \gamma^0$, showing the Purcell-enhanced linewidth of the molecule. When the cavity is far detuned ($\delta \gg \kappa$), $\gamma \approx \gamma^0$, revealing the molecular linewidth in free space. The shift in the center frequency $\delta\omega_0$ follows a dispersive lineshape with respect to $\delta$ and vanishes at zero detuning. When the cavity is far detuned ($\delta \gg \kappa$),

$$\delta\omega_0(\delta) \approx -\frac{\kappa\gamma_{\mathrm{cav}}}{4\delta} = -\frac{g^2}{\delta} \,, \tag{48}$$

recovering the well-known formula for the cavity-modified Lamb shift [27]. The dependences of $\gamma$ and $\delta\omega_0$ on $\delta$ are plotted in Fig. 7 (b) and (c).

### 4.3. Phase response

The scattering of light by an atom is also accompanied by a phase shift. The information on the phase can be used to detect photons non-destructively [40]. Here, we examine the phase shift a laser beam acquired after traversing the coupled molecule-cavity system.

The complex transmission coefficient $t$ of the coupled system can be expressed as

$$t = |t_0| \cdot |t'| \cdot e^{i(\phi_0 + \phi')} \,, \tag{49}$$
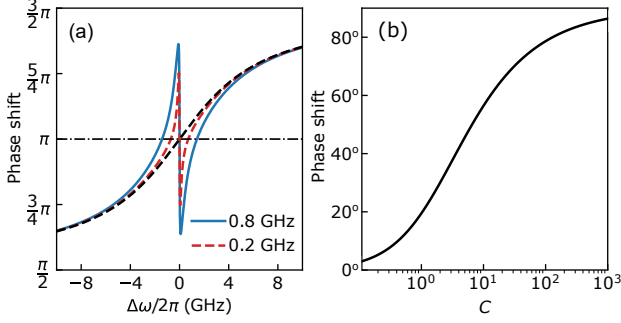
**Figure 8.** (a), Phase shift of light transmitted through the coupled system. The blue (red) line is for $\gamma_{\text{cav}}/2\pi = 0.8$ GHz (0.2 GHz) and $(\kappa, \gamma^0, \delta)/2\pi = (10, 0.04, 0)$ GHz. The dashed black line represents the phase shift of an empty cavity. The phase shift of resonant transmission through an empty cavity amounts to $\pi$ as marked by the dashed-dotted black line. (b), Maximal phase shift as a function of the cooperativity.

where $t'$ represents the term in the squared brackets of Eq. 43. $\phi_0$ denotes the argument of $t_0$ and represents the phase shift of transmission through an empty cavity. $\phi'$ stands for the additional phase shift due to the coupling to the molecule. The dashed black line in Fig. 8 (a) displays the phase shift of transmission through an empty cavity with $\kappa/2\pi = 5$ GHz. The phase of the resonantly transmitted light is shifted by $\pi$ from the incoming beam, which is marked by the dashed-dotted black line and originates from the minus sign in the expression of $t_0$ (see Eq. 42). The phase shift covers the range of $(\pi/2, 3\pi/2)$. The solid blue curve shows the phase shift $\phi_0 + \phi'$ when a molecule is coupled to the cavity with $(\gamma^0, \gamma_{\text{cav}})/2\pi = (0.04, 0.8)$ GHz. The molecule introduces a sharp change in phase with amplitudes of up to $\pm\pi/3$. The dashed red line displays the phase shift for a weaker molecule-cavity coupling with $\gamma_{\text{cav}}/2\pi = 0.2$ GHz. In this case, the phase is shifted by up to $\pm\pi/4$.

A simple analytical expression of the phase shift can be obtained in the limit $\kappa \gg \gamma$, where the approximation $\Delta\omega/\kappa \approx 0$ can be applied to obtain

$$\tan[\phi'(\Delta\omega)] \approx -\frac{1}{\Delta\omega \cdot \dfrac{2}{\gamma_{\text{cav}}} + \dfrac{1}{\Delta\omega} \cdot \dfrac{\gamma^0}{2} \cdot \left(1 + \dfrac{\gamma^0}{\gamma_{\text{cav}}}\right)} . \tag{50}$$

The maximal phase shift of

$$\max[|\phi'(\Delta\omega)|] = \arctan\left(\frac{1}{2}\sqrt{\frac{C^2}{C+1}}\right) \tag{51}$$

is achieved when $\Delta\omega = \pm\sqrt{\gamma^0(\gamma_{\text{cav}} + \gamma^0)/4}$, with $C = \gamma_{\text{cav}}/\gamma^0$ the cooperativity of the system. The maximal phase shift scales nonlinearly with $C$, as displayed in

Fig. 8 (b). To reach a phase shift close to $90°$, it is necessary to have $C$ in the order of $10^3$.

### 4.4. Saturation of the system

The efficient coupling of the molecule with the cavity also gives rise to strong optical nonlinearities. Consider a resonantly coupled system ($\delta = 0$, $\Delta\omega = 0$) and follow Ref. [35], the steady-state solutions for the atomic operators at an arbitrary incident power can be written as

$$s_z = \langle \sigma_z \rangle = -\frac{1}{1+S},$$

$$s = \langle \sigma_- \rangle = \sqrt{\frac{2}{\gamma_{\text{cav}}}} \frac{b_{\text{in}}}{1+S} \, \beta \,, \tag{52}$$

where $S = 4\beta^2|b_{\text{in}}|^2/\gamma_{\text{cav}}$ denotes the saturation parameter. Alternatively, $S$ can be expressed as

$$S = \frac{|b_{\text{in}}|^2/\gamma'}{\gamma_{\text{cav}}/(4\beta^2\gamma')} = \frac{n_{\text{in}}}{n_{\text{c}}}, \tag{53}$$

where $n_{\text{in}} = |b_{\text{in}}|^2/\gamma'$ represents the number of incident photons per Purcell-enhanced lifetime of the molecule and $n_{\text{c}} = \gamma_{\text{cav}}/(4\beta^2\gamma')$ denotes the critical photon number to reach $S = 1$ (i.e. the occupation probability of the excited-state is 25%).

Using the expression of the transmitted field $b_t$ (see Eq. 41), the transmitted power can be written as

$$\langle b_t^\dagger b_t \rangle = |b_{\text{in}}|^2 - 2|b_{\text{in}}|\sqrt{\frac{\gamma_{\text{cav}}}{2}} \cdot \text{Re}\left[\langle s \rangle\right] + \frac{\gamma_{\text{cav}}}{2}\langle s^\dagger s \rangle . \tag{54}$$

Combining Eq. 52 and Eq. 54, gives

$$\langle b_t^\dagger b_t \rangle = |b_{\text{in}}|^2 \cdot \left[\left(1 - \frac{\beta}{1+S}\right)^2 + \beta^2 \cdot \frac{S}{(1+S)^2}\right], \tag{55}$$

where the first term in the square brackets represents the coherent contribution to the transmitted power ($|\langle b_t \rangle|^2$) and the second term stems from its fluctuations ($\langle b_t^\dagger b_t \rangle - |\langle b_t \rangle|^2$). The steady-state transmission is then

$$T = \frac{\langle b_t^\dagger b_t \rangle}{|b_{\text{in}}|^2} = \left(1 - \frac{\beta}{1+S}\right)^2 + \beta^2 \cdot \frac{S}{(1+S)^2} . \tag{56}$$

Figure 9 displays $T$ as a function of $n_{\text{in}}$ for systems with different $\beta$. The transmission saturates gradually as the incident power increases. The critical photon numbers to reach $S = 1$ are marked by the colored arrows. In the regime of very high pump rates ($S \to \infty$), $s_z \approx 0$ and the occupation probability of the excited state is 50%. We note that a single photon
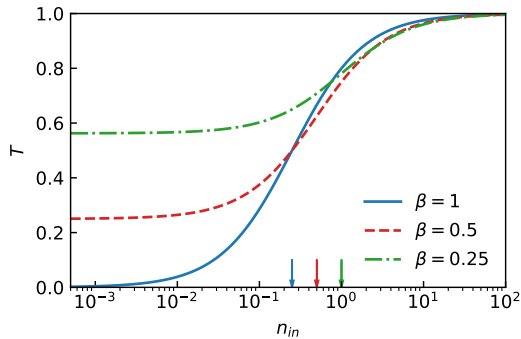
**Figure 9.** Saturation of the system. The vertical axis shows the resonant transmission of the coupled system. The horizontal axis denote the incident power in photon number per excited-state lifetime of the molecule. The critical photon numbers for three values of $\beta$ are marked by the correspondingly colored arrows.
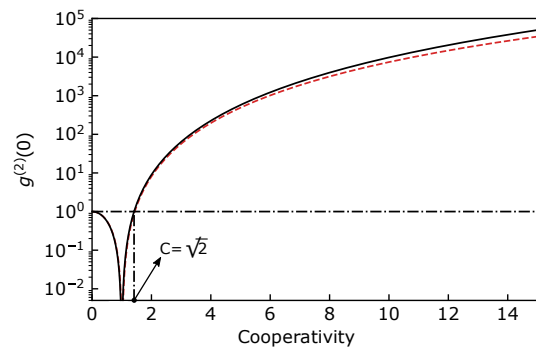
**Figure 10.** $g^{(2)}(0)$ of the intracavity field as a function of the cooperativity $C$. The dashed red line displays $g^{(2)}(0)$ calculated using Eq. 60, for a system with $(\gamma^0, \kappa)/2\pi = (0.04, 3)$ GHz. The solid black line shows the calculation using Eq. 62. The dashed-dotted lines mark the position of $C = \sqrt{2}$ and $g^{(2)}(0) = 1$.

is predicted to be enough to act as a $\pi$-pulse and completely invert a two-level system [5]. This is a transient process and requires the spatial and temporal modes of the photon to match the time-reverse of a spontaneously emitted photon. The complete inversion of a two-level system is not possible in the steady-state. Considering a perfect coupling ($\beta = 1$) in the present model, the minimal critical photon number to reach $S = 1$ is 0.25 [35].

### 4.5. Photon statistics of the transmitted light

An emitter placed in a cavity not only modifies the cavity's spectrum, but also gives rise to dynamic effects which can be observed in the photon statistics of the intracavity and transmitted fields [41–43]. In contrast to the structural effects such as the spectral modifications, which can be described by classical models [44, 45], the dynamic effects can result in nonclassical photon correlations which can only be explained quantum mechanically [43].

We start by briefly reviewing the theoretical model developed in Ref. [43]. The model considers a two-level emitter resonantly coupled to a cavity mode and driven by a weak resonant laser field. In this regime, one can assume the system to have at most two excitations and neglect the higher excitation states. A master equation approach was employed to describe the temporal evolution, which can be solved for a truncated expansion of the joint density matrix. The steady-state wavefunction of the system expanded up to two excitation quanta can be expressed as

$$|\psi\rangle = |g,0\rangle + A|g,1\rangle$$
$$+ B|e,0\rangle + (A^2/2)pq|g,2\rangle + ABq|e,1\rangle, \quad (57)$$

where,

$$A = (2E/\kappa)/(1+C),$$
$$B = -(2g/\gamma^0) \cdot A,$$
$$p = 1 - C/(1+\gamma^0/\kappa),$$
$$q = (1+C)/[1+C-C/(1+\gamma^0/\kappa)], \quad (58)$$

and $E$ is the amplitude of the intracavity driving field.‖ The normalized second-order intensity-correlation function of the intracavity field can be calculated with

$$g^{(2)}(\tau) = \frac{\langle\psi|a^\dagger(0)a^\dagger(\tau)a(\tau)a(0)|\psi\rangle}{(\langle\psi|a^\dagger(0)a(0)|\psi\rangle)^2}. \quad (59)$$

Using the expression of the steady-state wavefunction $|\psi\rangle$ in Eq. 57, one arrives at

$$g^{(2)}(\tau) = |1 + (pq-1)\exp\left(-\frac{\kappa+\gamma^0}{4}\tau\right)\cdot$$
$$(\cosh M\tau + \frac{\kappa+\gamma^0}{4M}\sinh M\tau)|^2, \quad (60)$$

with $\tau > 0$ the time delay between the two detectors and $M = \sqrt{[(\kappa-\gamma^0)/4]^2 - g^2}$. Note that this expression is derived for the intracavity field, but the same result also applies to the transmitted field, since the field operators only differ by a scaling factor of $\sqrt{\kappa/2}$, which cancels in Eq. 59.

In cases of non-zero cavity and laser frequency detunings, the corresponding steady-state wavefunction can be derived from the master equation, which results in the same expressions as Eqs. 57-60 with the following

---

‖We note the differences in the conventions of $C$ and $\kappa$ in Ref. [43] and this tutorial: $C$ and $\kappa$ quoted in this tutorial correspond to $2C$ and $2\kappa$ in Ref. [43], respectively.

transformations

$$\kappa \to \kappa + 2i(\Delta\omega + \delta) \,,$$
$$\gamma^0 \to \gamma^0 + 2i\Delta\omega \,. \tag{61}$$

We now focus on the intensity correlations at zero time delay. Using the approximation $\gamma^0/\kappa \ll 1$, we can simplify Eq. 60 to

$$g^{(2)}(0) = (1 - C^2)^2 \,. \tag{62}$$

The dependence of $g^{(2)}(0)$ on $C$ is displayed in Fig. 10. The solid black curve in the figure shows the results calculated using Eq. 62. The dashed red curve in the same figure displays $g^{(2)}(0)$ calculated using Eq. 60, for a system with $(\kappa, \gamma^0)/2\pi = (3, 0.04)$ GHz. The two curves only differ slightly in the limit of large cooperativities.

For a system with cooperativity factor in the range $(0, \sqrt{2})$, the intracavity field is antibunched at zero time delay. When $C$ is larger than $\sqrt{2}$, the intracavity field is bunched and $g^{(2)}(0)$ increases approximately quartically with $C$. In the special case of $C = 1$, the intracavity field is perfectly antibunched, implying that only single photons can traverse the system. The system thus functions as a single-photon filter.

## 5. Integrating single molecules to a cryogenic Fabry-Perot cavity

Pioneering experiments of cavity QED were carried out with atoms in ultrahigh vacuum and macroscopic Fabry-Perot cavities [26, 27, 46]. Incremental developments in the cavity design and the manipulation of atoms have led to the strong coupling of a single atom to a cavity mode at both microwave and optical frequencies [47, 48]. The success of this approach benefited greatly from the development of super-polished substrates and high-reflectivity coatings using superconductors [47] or multilayer dielectrics [49, 50]. For cavities operating at optical frequencies, finesse of $2 \times 10^6$ and quality factor of up to $10^{10}$ were reported [49].

Our approach is to achieve a small mode volume by miniaturizing the Fabry-Perot cavity. By fabricating curved mirrors with small radius of curvature (ROC) on micro-pedestals [51–56], Fabry-Perot microcavities with mode volume smaller than one $\lambda^3$ have been achieved [56]. The highlights of open Fabry-Perot microcavities are their easy tunability, scannablity and the flexibility of adapting different species of emitters. We use a hemispherical cavity consisting of a planar mirror and a curved micromirror, as shown in Fig. 11. In the Gaussian approximation, the cavity mode has its waist at the planar mirror, where a thin molecule
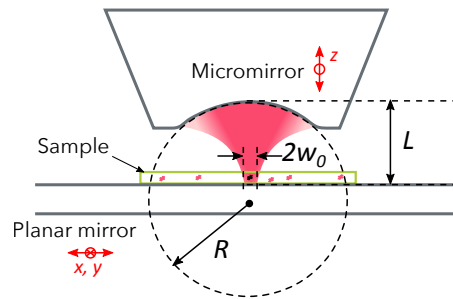


**Figure 11.** A hemispherical microcavity consisting of a planar mirror and a curved micromirror. A thin layer doped with single emitters is placed on the planar mirror. The resonance frequency of the cavity can be tuned by adjusting the micromirror in the axial ($z$) direction. The planar mirror can be scanned laterally (along the $x$-$y$ plane) to deterministically position an emitter at the center of the mode.

doped crystal can be placed. The mode volume of a hemispherical Fabry-Perot cavity can be estimated using [53]

$$V = \frac{\pi}{4} w_0^2 L, \tag{63}$$

where $L$ is the cavity length and $w_0 = (\lambda^2 LR/\pi^2)^{1/4}$ is the mode waist ($1/e$ half width) , with $R$ the ROC of the curved mirror. In order to achieve a small $V$, it is necessary to reduce both the ROC and the cavity length.

### 5.1. Micromirror fabrication and cavity assembly

An established technique for fabricating curved micromirrors is $CO_2$-laser ablation, where a single (or a few) high energy laser pulse is used to produce a Gaussian-shaped concave structure on a glass substrate [51–53]. This method can result in very smooth surfaces with root-mean-square surface (RMS) roughness less than $0.2$ nm [52]. The high surface quality allows the adoption of high-reflectivity dielectric coatings, with which cavities with finesse larger than $10^5$ were reported [53, 57].

We use focused-ion-beam (FIB) milling [58] to fabricate micromirrors for the experiment. FIB is a technique capable of fabricating mirrors with ROCs below $10\,\mu$m and offers nanometer-level topographic control on various materials [56, 59, 60]. Figure 12 (a) displays a scanning electron microscope (SEM) image of a micromirror machined at the cleaved end of a single-mode fiber made of fused silica. The black line in Fig. 12 (b) represents a cross sectional atomic force microscope (AFM) image across the center of the mirror, showing a hemispherical shape with an opening diameter of about $7\,\mu$m and depth of $500$ nm. The green curve represents a fit of the central region to a circle, yielding a ROC of $10.0\,\mu$m. The maximal
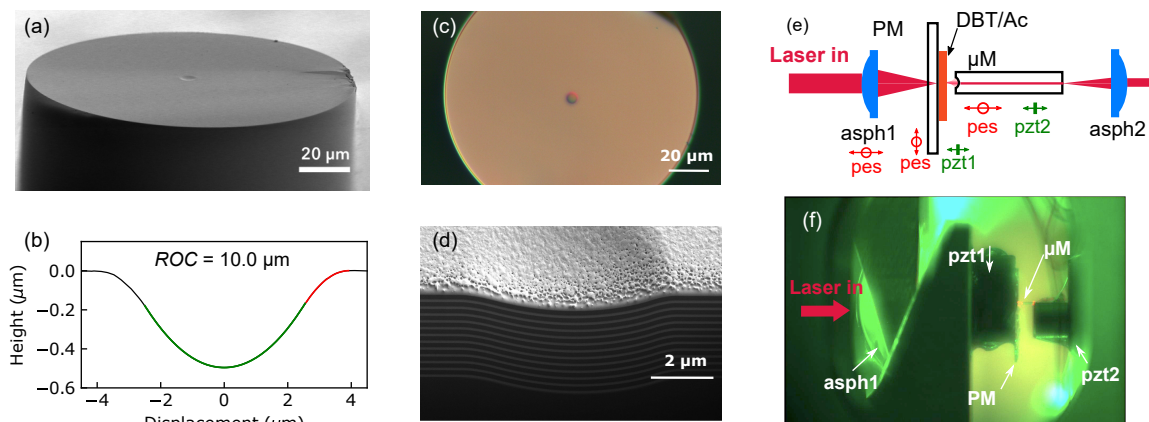
**Figure 12.** (a), An SEM image of the cleaved end of a fused-silica fiber. A micromirror was fabricated at the center. (b), The black line shows an AFM cross sectional measurement across the center of the micromirror shown in (a). The green and the red lines represent fits to a circle. (c), Optical microscope image of a micromirror after coated with dielectric multilayers. (d), An SEM image of the multilayer dielectric coating on the micromirror after cut using FIB. The mirror has a radius of curvature of $10\,\mu m$ and a depth of $500\,nm$. The coating consists of 12 alternating layers of $Nb_2O_5$ and $SiO_2$. The apparent surface roughness is caused by a metallic coating necessary for imaging with the SEM. (e), Schematic of the microcavity assembly. The cavity is formed by a micromirror and a planar mirror with a thin Ac crystal attached to it. Laser light is coupled into the cavity through an aspheric lens (asph1) and the light transmitted through the fiber is collected by a second aspheric lens (asph2). The red arrows denote the degrees of freedom for coarse alignment using three slip-stick nano-positioners (pes). The green arrows indicate the fine cavity length adjustments with two ring piezoelectric transducers (pzt1, pzt2). PM, planar mirror; $\mu$M, micromirror; DBT/Ac, DBT-doped thin anthracene crystal. (e), A photograph of the cavity assembly at $4.2\,K$, taken through a side viewport of the cryostat.

deviation of the measured data from the circular fit is about $1\,nm$ and the root-mean-square roughness of the mirror is less than $0.4\,nm$, which is limited by the resolution of the AFM. We note that it is not necessary to involve an additional polishing step to achieve this surface smoothness, since FIB provides an effective polishing due to the dependence of the sputtering rate on the incident angle of the ion beam [59]. The red curve in Fig. 12 (d) shows a circular smoothing pattern with a ROC of $5.7\,\mu$m. This was implemented to avoid sharp features around the edge, so to ease the adoption of a multilayered dielectric coating.

After FIB machining, the mirrors are coated with a dielectric layer to achieve a high reflectivity. Figure 12 (c) displays an optical microscope image of a micromirror after being coated with dielectric layers. An SEM image of the dielectric coating after being cut by the FIB is shown in Fig. 12 (d). The dielectric coating consists of alternating $\lambda/4$-thick layers of $Nb_2O_5/SiO_2$ or $TiO_2/SiO_2$. Twelve such bilayers are deposited on the substrate to reach reflectivities of up to 99.995%.

The microcavity is hosted on an insert of a liquid helium cryostat. A schematic of the cavity assembly is shown in Fig. 12 (e). The planar mirror is mounted on a slip-stick piezoelectric slider (PES) which positions the molecular sample in the transverse direction. The micromirror is machined at the cleaved end of a single mode fiber, sits on a second PES and travels along

the axial direction of the cavity. Each of the cavity mirrors is glued on a ring piezoelectric transducer (pzt1, pzt2) to facilitate the fine adjustment of the cavity length. The incident laser beam is coupled to the cavity using an aspheric lens (asph1: NA=0.5), which is mounted on a third PES to adjust the focus of the incoming beam. A second aspheric lens (asph2: NA=0.2) is mounted at the transmission side of the fiber to collimate the transmitted light from the fiber. Figure 12 (f) shows a side-view photograph through the window of the cryostat when the insert is cooled to $4.2\,K$.

### 5.2. Single-molecule sample preparation and detection

The experiments are carried out with dibenzoterrylene (DBT) molecules doped in thin anthracene (Ac) crystals. The molecular structures of DBT and Ac are illustrated in the upper panel of Fig. 13 (a). A DBT molecule can be inserted into the Ac lattice by substituting three Ac molecules in two possible insertion sites [23]. Photophysics of DBT molecules in these two sites were studied in Ref. [36]. We used molecules in the main insertion site with the 00ZPL ($S_0$ to $S_1$) transition lying around $784\,nm$.

We fabricate DBT-doped Ac crystals using a vapor-phase growth method [61]. The thickness of the Ac crystals fabricated using this method lies in the range from 0.1 to $5\,\mu$m. We obtain typically 20 to 50 molecules in a confocal spot ($\sim 700\,nm\times700\,nm$).
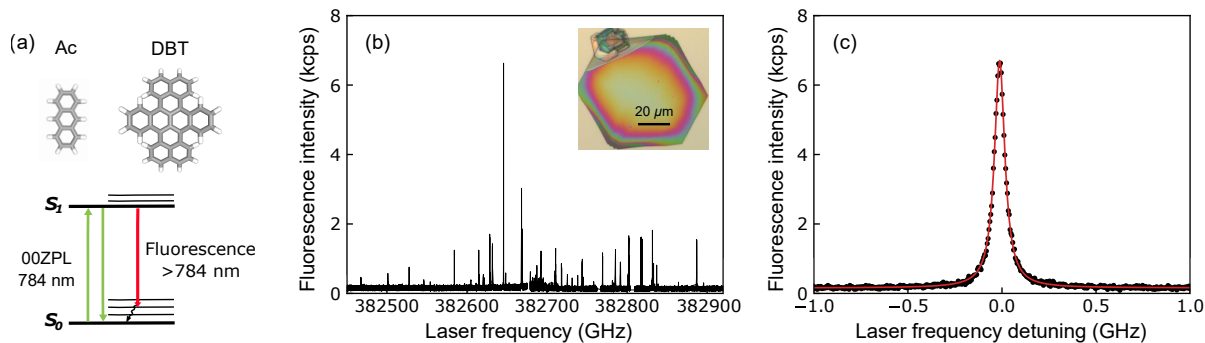
**Figure 13.** (a), Upper: molecular structures of Ac and DBT. Lower: a simplified energy diagram of a DBT molecule (lower) showing the wavelength of the 00ZPL transition and the red-shifted fluorescence. (b), Inhomogeneous broadening of DBT molecules in Ac. The plot shows fluorescence excitation spectrum measured on a confocal spot on the Ac crystal. Each peak represents the 00ZPL transition of a single molecule. The inset shows an optical microscope image of a DBT-doped Ac crystal. Individual sharp peaks represent single molecules. (c), A close-up of the spectrum of a single molecule. The red line shows a fit to a Lorentzian function.

Single-molecule detection is possible by exploiting the inhomogeneous broadening of the molecular transition frequencies. When cooled down to $T \sim 4\,\mathrm{K}$, the 00ZPL of DBT molecules narrows down to their Fourier limit of about 40 MHz [23, 62]. Each molecule experiences a slightly different local environment such as strain and electric field and acquires a different shift in its energy levels. Figure 13 (b) displays the measured fluorescence intensity from a confocal spot on the crystal, when the frequency of a narrow-linewidth ($< 1\,\mathrm{MHz}$) excitation laser is tuned across the inhomogeneous broadening of the 00ZPLs. Each of the sharp peaks represents the 00ZPL transition of an individual molecule. A close-up of the fluorescence spectrum of a single molecule is displayed in Fig. 13 (c). The red line represents a fit to a Lorentzian function, with a FWHM of $66.8\pm0.2\,\mathrm{MHz}$. In this example, the linewidth of the Lorentzian profile is larger than the natural linewidth ($\sim 40\,\mathrm{MHz}$), due to a slight power broadening.

## 6. Observation of coherent light-molecule coupling

The cavity assembly including the molecule doped crystal are cooled to 4.2 K in a liquid helium cryostat. At this temperature, the finesse of the cavity is measured to be around 19 000 at 784 nm. We identify a suitable molecule by monitoring the transmission spectrum while tuning the cavity resonance across the inhomogeneous broadening of the molecules. In the following, we present the observations of the coherent coupling of a single molecule to the cavity mode.

### 6.1. Resonant response, Purcell enhancement and Lamb shift

The blue dots in Fig. 14 (a) show the measured transmission spectrum of an empty cavity. The red dots show the transmission spectrum when the cavity is tuned on resonance with the molecule. The dip with a FWHM of around 600 MHz is a result of destructive interference of the molecular scattering with the cavity mode, as explained in section 4. The black dots display the background level of the measurement. The solid lines show theoretical fits. A quantitative comparison of the three curves suggests that the presence of the molecule attenuates the resonant transmission of the cavity by more than 99%. This measurement is performed by detecting the cross-polarized reflection (CPR) signal from the cavity [62]. The same measurements are performed on the light transmitted through the single-mode fiber hosting the micromirror, as shown in Fig. 14 (b). The solid lines represent theoretical fits using the same group of cavity-QED parameters as in (a). Due to the non-ideal mode matching between the cavity mode and the guiding mode of the fiber, the signals show a lower signal to noise ratio. Nevertheless, the two sets of measurements provide the same information of the system.

The measured reflection spectra are presented in Fig. 14 (c). The blue dots display the cavity resonance. The black dots show the reflected intensity when the cavity resonance is detuned. The empty cavity resonance does not dip to zero due to an imperfect mode matching and the effects of residual vibrations in cavity length. The red dots show the reflection spectrum of the coupled system, revealing a nearly perfect dipole-induced reflection.
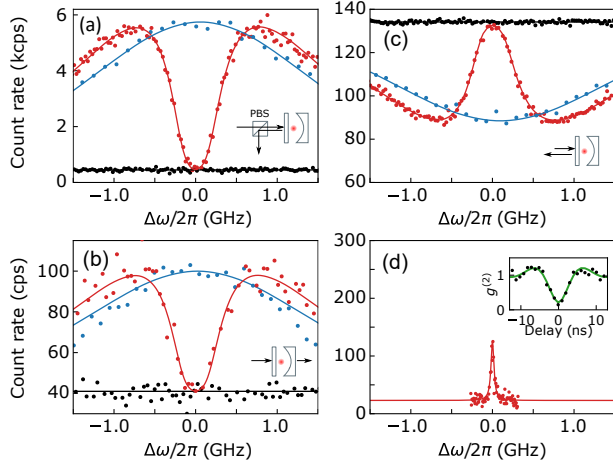
**Figure 14.** (a), Transmission spectrum of the coupled system measured via cross-polarized reflection. Blue: the CPR spectrum of the cavity when detuned from the molecule. Red: the CPR spectrum of the resonantly coupled molecule-cavity system. Black: intensity of the laser beam reflected from the cavity when it is detuned from the cavity and the molecular resonances, providing the background level. PBS: polarization beamsplitter. (b), Same as in (a) but measured on the light transmitted through the single-mode fiber. (c), Same as in (a) but measured in reflection without a cross-polarizer. (d), Fluorescence excitation spectrum of the molecule recorded when the cavity resonance is far detuned. The inset shows an intensity correlation of the fluorescence signal. A clear antibunching at zero time delay confirms that the observed signal comes from a single molecule. All solid curves denote theoretical fits.

To verify that the signals originate from a single molecule, a fluorescence excitation measurement is performed. The red dots in Fig. 14 (d) display the fluorescence spectrum when the cavity resonance is far-detuned. The solid red line represents a Lorentzian fit with a FWHM of $44 \pm 5$ MHz, revealing the unperturbed linewidth of the molecule and matching the typical values of DBT molecules in Ac crystals [36, 62–64]. The low signal to noise ratio is a result of the high reflectivity of the dielectric mirrors. The inset in Fig. 14 (d) displays the measured second-order intensity-correlation function (black dots) at the fluorescence peak. A theoretical fit is shown by the green line. The resulting $g^{(2)}(0) = 0.21 \pm 0.06$ confirms that the observed signal is from a single molecule. The oscillations at the shoulders of the signal are signatures of Rabi-oscillations [65].

The fine frequency tunability of the cavity allows us to perform quantitative studies of the Purcell effect and modifications to the Lamb shift [38, 39, 66]. Figures 15 (a), (b) show the extracted frequency shift $\delta\omega_0$ and linewidth $\gamma$ of the molecule as a function of the molecule-cavity detuning $\delta$. The frequency of the 00ZPL transition is shifted towards blue or red, depending on the sign of $\delta$. The measured frequency
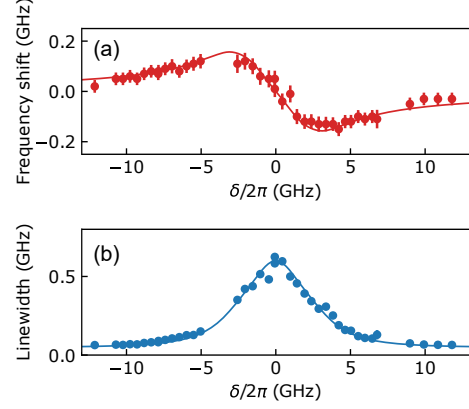


**Figure 15.** Frequency shift of the 00ZPL transition (a) and molecular linewidth (b) as a function of molecule-cavity detuning. The colored dots represent the quantities extracted from the measurements. The solid lines show the theoretical predictions.

shifts are up to $\pm 150$ MHz. Purcell enhancement is evidenced by the broadening of the molecular linewidth from $\gamma^0 = 44 \pm 5$ MHz for a detuned cavity to $\gamma' = 604 \pm 21$ MHz when the cavity is on resonance.

### 6.2. Onset of strong coupling

We determine the cavity-QED parameters of the system by comparing the molecular linewidths $\gamma^0$ and $\gamma$. Following the theory introduced in section 4, we express $\gamma^0$ and $\gamma'$ as

$$\gamma^0 = \gamma_{\mathrm{red}} + \gamma_{\mathrm{zpl}} \,,$$
$$\gamma' = \gamma_{\mathrm{red}} + (1 + F) \cdot \gamma_{\mathrm{zpl}} \,. \tag{64}$$

For DBT molecules embedded in Ac crystals, the typical relation between the two decay rates is $\gamma_{\mathrm{red}} \approx 2\gamma_{\mathrm{zpl}}$ [63]. This allows us to deduces the Purcell factor of our system, giving $F = 38 \pm 5$. The cooperativity $C$, which quantifies the cooperative emission into the cavity mode, can be calculated as

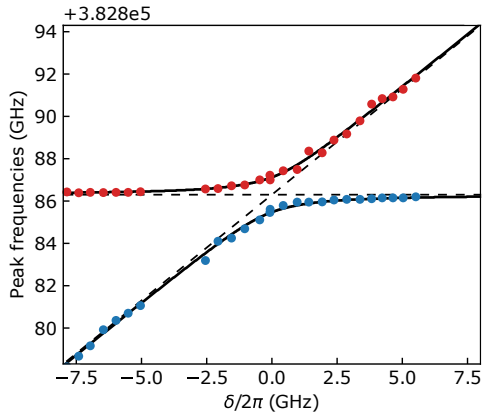$$C = \frac{F \cdot \gamma_{\mathrm{zpl}}}{\gamma^0} \,, \tag{65}$$

resulting in $C = 12.7 \pm 1.6$.

The $\beta$-factor associated with the 00ZPL ($\beta_{\mathrm{zpl}}$) and the cavity-modified branching ratio $\alpha'$ can be calculated using

$$\beta_{\mathrm{zpl}} = \frac{F \cdot \gamma_{\mathrm{zpl}}}{(F + 1) \cdot \gamma_{\mathrm{zpl}}} = \frac{F}{F + 1} \,,$$
$$\alpha' = \frac{(F + 1) \cdot \gamma_{\mathrm{zpl}}}{(F + 1) \cdot \gamma_{\mathrm{zpl}} + \gamma_{\mathrm{red}}} \approx \frac{F + 1}{F + 3} \,. \tag{66}$$

We obtain $\beta_{\mathrm{zpl}} = 97.4 \pm 0.3\%$ and $\alpha' = 95.1 \pm 0.6\%$. The $\beta$-factor of the overall emission is $\beta = \beta_{\mathrm{zpl}} \cdot \alpha' \approx 93\%$.

**Figure 16.** Frequency of the higher- (red dots) and lower- (blue dots) energy transmission peaks as a function of the molecule-cavity detuning. Black lines present the same quantities extracted from the theoretical spectra.

The three parameters close to unity indicate that the cavity changes the molecule to a nearly ideal two-level atom, and the emission of the molecule is strongly directional, i.e. preferentially into the cavity mode.

Estimating the Purcell factor using Eq. 14 and considering a mode volume of $4.4\lambda^3$, an effective refractive index $n = 1.8$ would result in $F = 355$. The discrepancy of the measured value of $F = 38$ from the ideal value is the result of several non-ideal factors. First, the misalignment of the DBT transition dipole to the **b**-axis of the Ac crystal [62] can lead to a reduction of $F$ by $\sim 20\%$. Second, a lack of control over the depth of the molecule in the crystal can introduce an offset of the molecule from the antinode of the cavity mode. An offset of 50 nm in depth would result in a reduction by a factor of 2. A displacement of about 80 nm would be sufficient to reduce the expected Purcell factor to the experimental value.

In Fig. 16, we plot the positions of the higher- and lower-energy transmission maxima as a function of the molecule-cavity detuning. The solid lines display the same quantities extracted from the theoretical spectra. The amount of splitting between the two maxima at zero detuning equals $2g$, allowing us to obtain $g/2\pi = 0.79 \pm 0.3$ GHz.

Mode-splitting in transmission is usually associated with strong coupling. However, a more decisive signature for entering the strong coupling regime is the bifurcation of eigenstates [33, 34], which occurs at the exceptional point (EP) of $g = (\kappa - \gamma^0)/4$ and is observable in fluorescence, rather than in transmission [33, 34]. In our system, $g \approx (\kappa - \gamma^0)/4$, implying that the system is at the onset of strong coupling. To better assert our experimental regime and visualize the

transition from weak to strong coupling, we plot the transmission and fluorescence spectra of the system while scaling the cavity linewidth from its experiment value and keeping the value of $g$ unaltered. This scaling corresponds to an experimental situation, where the mode volume of a cavity is kept constant but the finesse is increased or decreased.

Figures 17 (a), (b) display the calculated transmission and fluorescence spectra of the system with the horizontal axis denoting the linewidth of the cavity. The fluorescence spectra $L(\Delta\omega)$ are obtained using $L(\Delta\omega) = 1 - T(\Delta\omega) - R(\Delta\omega)$. One notices that the splitting of the transmission spectra appears independent of the cavity linewidth, even when the system is deeply in the weak-coupling regime (see (c)). The location of the EP is marked out by the solid white line in (a), and the corresponding transmission spectrum is represented by the blue line in (e). The measured transmission spectrum of the system is displayed by the gray dots in (e). The close agreement between the experimental and the calculated EP spectrum confirms that our system is at the onset of the strong coupling. The small offsets at the shoulders of the spectra are a result of vibrational broadening of the cavity resonance, which leads to deviations of the measured spectrum from a Lorentzian profile. The fluorescence spectra (see (b) and (h)-(l)) evolve differently from the transmission spectra. In the weak-coupling regime, the fluorescence spectrum is a Lorentzian profile with linewidth the Purcell-enhanced linewidth of the molecule (see (h), (i)). At the EP, the fluorescence spectrum becomes flat-topped (see (j), and Ref. [32]). After entering the strong coupling regime, the fluorescence spectrum is split into two peaks, as shown by (k), (l).

### 6.3. Phase-shift

As discussed in section 4, the scattering of light by a quantum emitter is accompanied by a phase shift. To measure the phase shift introduced by the molecule, we follow the scheme introduced in Ref. [67] and employ a two-frequency common-path interferometer. In brief, two laser beams with electric fields $|E_1| \cdot e^{-i\omega_1 t}$ and $|E_2| \cdot e^{-i(\omega_2 t + \phi_0)}$ generated using an acousto-optic modulator are combined and forwarded to the cavity. Here, $\omega_{1,2}$ denote the frequency of the two laser beams, $|E_{1,2}|$ represent their electric field amplitudes and $\phi_0$ denote their initial phase difference. Before entering the cavity, a beam sampler reflects part of the light onto a fast photodiode. The intensity on the photodiode can be written as

$$
\begin{aligned}
I_{\text{bs}} = R_{\text{bs}} \cdot \{ &|E_1|^2 + |E_2|^2 \\
&+ 2|E_1 \cdot E_2| \cos[(\omega_2 - \omega_1)t + \phi_0] \}, \quad (67)
\end{aligned}
$$
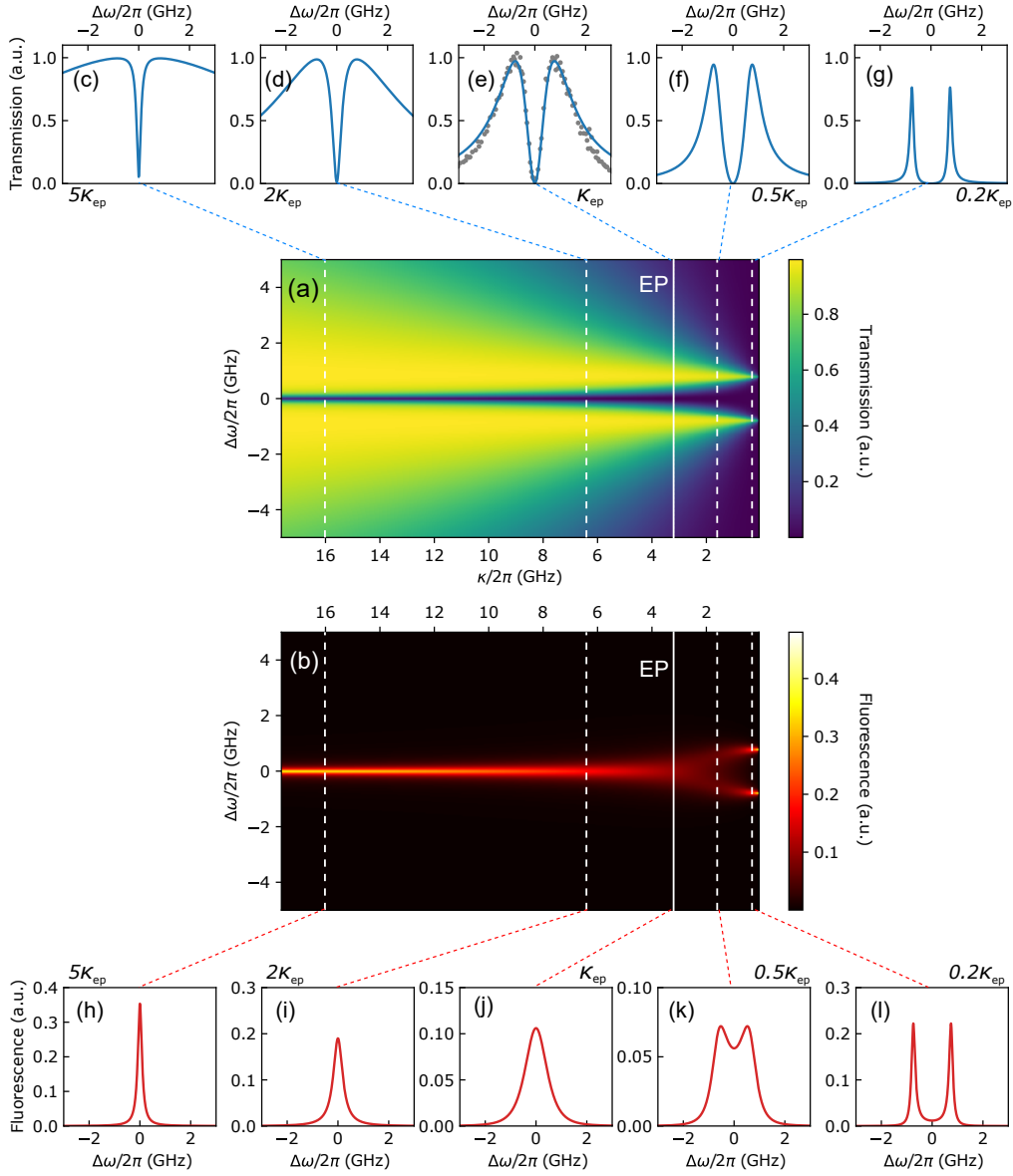
**Figure 17.** (a), (b), Calculated transmission and fluorescence spectra of the coupled system as a function of the cavity linewidth $\kappa$. The solid white lines mark the location of the EP with cavity linewidth $\kappa_{\mathrm{ep}}$. (c)-(g), Cross sectional transmission spectra at cavity linewidths displayed at the bottom of each plot and marked by the dashed white lines in (a). The experimentally measured transmission spectrum is superposed on the calculated spectrum at the EP, shown by the gray dots in (e). The lower panel (h)-(l) displays the same but for the fluorescence spectra.

where $R_{\mathrm{bs}}$ denotes the reflectivity of the beam sampler. The intensity consists of two constant terms and an oscillation term at frequency $(\omega_2 - \omega_1)$ with starting phase $\phi_0$. The complex transmission coefficient of the cavity at $\omega_{1,2}$ can be expressed as $t_{\omega_{1,2}} = |t_{\omega_{1,2}}| \cdot e^{-i\phi_{\omega_{1,2}}}$. The intensity of the light transmitted through the cavity is then

$$
\begin{aligned}
I_{\mathrm{t}} =& (1 - R_{\mathrm{bs}}) \cdot \{ |t_{\omega_1} E_1|^2 + |t_{\omega_2} E_2|^2 \\
& + 2 |t_{\omega_1} E_1 \cdot t_{\omega_2} E_2 \cdot| \cdot \cos[(\omega_2 - \omega_1)t \\
& - (\phi_{\omega_2} - \phi_{\omega_1}) + \phi_0] \} ,
\end{aligned} \tag{68}
$$

which also consists of two constant terms and an oscillation term at frequency $(\omega_2 - \omega_1)$. The starting phase of the oscillation is shifted by $\Delta\phi = \phi_{\omega_2} - \phi_{\omega_1}$ with respect to the initial phase difference $\phi_0$. The phase shift imprinted on the two beams is thus mapped onto the phase of the oscillation signal.

We measure the phase shift of the oscillation signal using time-correlated single-photon counting [68] with the trigger signal generated by the fast photodiode. In Fig. 18, the phase shift of a single laser beam is displayed. The red dots represent the measured phase
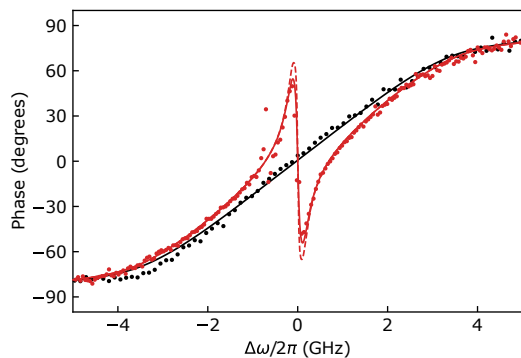
**Figure 18.** Phase shift of a laser beam by a single molecule. Red dots display the measured phase shift on a single laser beam and the solid red line represents the theoretical prediction accounting for the effect of saturation broadening. The dashed red line shows the predicted phase shift of a laser beam in the weak-excitation limit. The phase shift of an empty cavity is shown by the black dots (extracted from the measurement) and the black line (theoretical prediction).



**Figure 19.** Saturation of the coupled molecule-cavity system. (a)-(d), Transmission spectra of the system at different incident laser powers. The black dots represent the measured data and red curves show theoretical fits. The dashed green lines stand for the transmission spectra of an empty cavity, calculated using the fit parameters. The blue signals display the background levels. The incident laser powers are displayed in the legend.
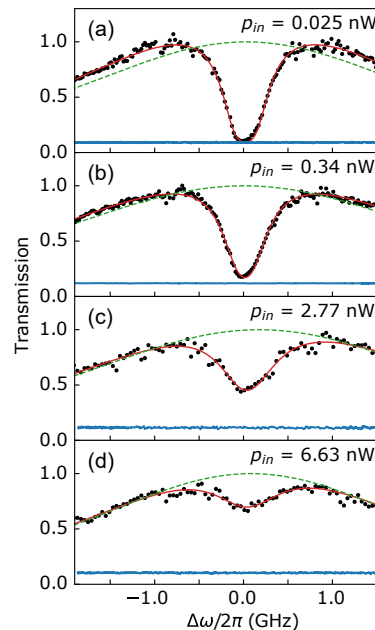
shift of a single laser beam traversing the coupled molecule-cavity system. The black dots show the same but for an empty cavity. The solid lines represent theoretical predictions. The red dashed line displays the phase shift on a single beam when assuming no power broadening of the molecule, allowing us to deduce phase shifts up to $\Delta\phi = \pm 66°$.

## 7. Single-photon nonlinear medium

Nonlinear optical experiments are typically performed with intense lasers and bulk materials [69]. Bringing nonlinear optics to the level of single photons holds great promises for quantum information applications [8, 70–72]. Such strong nonlinear interactions can be mediated by a two-level atom efficiently coupled to an optical mode [9, 71–73].

### 7.1. Saturation of the system

We characterize the nonlinear response of the coupled system by measuring the saturation effects in the transmission spectrum. In Fig. 19 (a)-(d), the black dots display a series of transmission spectra measured at different incident laser powers. The red lines stand for the theoretical fits and the dashed green lines represent the transmission spectra of an empty cavity. The background level for each measurement is shown by the signal in blue. At low incident powers, the coherent interaction modifies the transmission spectrum of the cavity significantly, leading to a strong attenuation of the resonant transmission (see (a), (b)). The molecule is gradually saturated as the laser power increases, accompanied by a reduction of the extinction signal (see (c), (d)). In this set of measurements, the

highest laser power delivered to the cryostat is 6.63 nW. At this power, we start to notice sudden jumps of the cavity length which cannot be compensated by the active feedback loop. This might suggest a local heating effect within the cavity. In any case, the upper limit of transmission is set by the empty cavity and the presented measurements already show a clear trend of saturation.

The incident laser power can be calibrated to the photon flux $n_{in}$ through the cavity per excited-state lifetime of the molecule. To do so, we start from the measured laser powers, account for the transmission of the cryostat-windows ($\sim$87%), the incoupling efficiency to the cavity ($\sim$10%) and the Fourier-limited lifetime of the molecule (264 ps). One photon per excited-state lifetime of the molecule translates to 11 nW of incident power in front of the cryostat. The incoupling efficiency is measured by monitoring the depth of the reflection dip from an empty cavity. This number is limited by the vibrational broadening and a polarization offset of the incident laser beam to allow for cross-polarized detection. When the incoming polarization is aligned to the cavity mode, the incoupling efficiency can be increased to $\sim$34%.

Figure 20 displays the resonant transmission of the coupled system as a function of the laser power. The
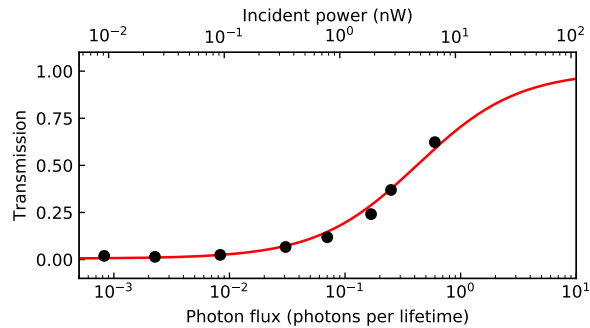
**Figure 20.** Resonant transmission of the system as a function of pump power. The upper horizontal axis presents the incident power before the cryostat window. The lower horizontal axis shows the estimated photon flux at the molecule per Purcell-enhanced lifetime. Black dots display the measured data. The red line represents a theoretical fit.

upper horizontal axis displays the measured incident powers in front of the cryostat, while the lower horizontal axis shows the calibrated photon flux per Purcell-enhanced lifetime of the molecule. The red line represents a theoretical fit using

$$T = \left(1 - \frac{\beta}{1+S}\right)^2 + \beta^2 \cdot \frac{S}{(1+S)^2}. \qquad (69)$$

Here, $S = n_{\mathrm{in}}/n_{\mathrm{c}}$ is the saturation parameter with $n_{\mathrm{c}}$ the critical photon number to reach $S = 1$. The fit gives $n_{\mathrm{c}} = 0.44$. With one incident photon per lifetime, the system is expected to reach $S \approx 2.3$. This is a direct indication of the single-photon nonlinearity of the system.

### 7.2. Resonant transmission: strong photon-bunching

A single-photon nonlinear medium responds differently to Fock-states of different photon numbers. When sending coherent states of light through the system, the transmitted light is expected to show non-Poissonian photon statistics. In section 4, we introduced the theoretical model for describing the photon statistics of the transmitted light. The modification of photon statistics results from the dynamic exchange of excitation between the emitter and the cavity [41–43].

We first set both the cavity and the laser frequencies on resonance with the molecule. The light transmitted through the system is sent to a Hanbury Brown and Twiss (HBT) setup consisting of a 50:50 beamsplitter and two fast avalanche photodetectors (APDs) [74]. The black dots in Fig. 21 (a) display the measured second-order correlation as a function of the time delay $\tau$ between the signals from the two APDs. A strong photon bunching at zero time delay is observed with a peak height of $g^{(2)}(0) \approx 21$. As explained in section 4,
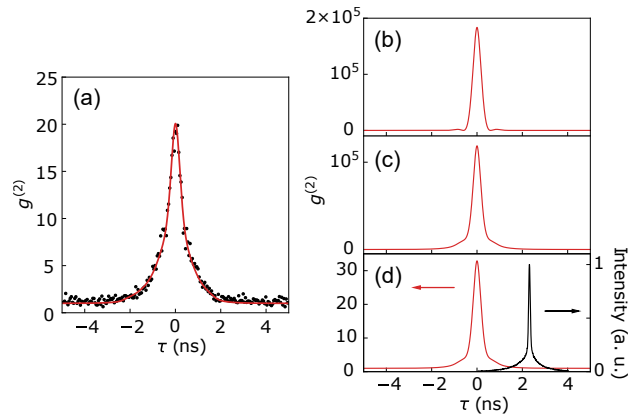


**Figure 21.** Intensity-autocorrelation function $g^{(2)}(\tau)$ of the resonantly transmitted light. (a), The black dots display the measured data, showing photon bunching with a maximal value of 21. The red line represents a theoretical fit considering the effects of vibrational broadening, background light and the instrument response function. (b), $g^{(2)}(\tau)$ calculated using the fit parameters but excluding the three factors mentioned above. (c), Same as in (b) but including the vibrational broadening. (d), Same as in (b) but including vibrational broadening and background light. The signal in black displays the instrumental response function. The offset of about 2 ns is added intentionally.

the origin of photon bunching in the regime of $C > \sqrt{2}$ is a higher two-photon transmission probability than that for single-photons. As a result, the probability of finding two-photon states in the transmitted light is higher than that given by Poissonian statistics.

An estimation using Eq. 62 yields $g^{(2)}(0) \approx 25700$ for $C = 12.7$, which is much larger than the observed value. Indeed, a few extra factors need to be considered to explain the observed signal. First, the vibrational perturbations to the cavity length lead to a change in the molecule-cavity detuning during the measurement. Second, the instrumental response function broadens and reduces the amplitude of the bunching peak. Lastly, Poissonian background light on the detectors lifts the background level of the $g^{(2)}$-signal. The red solid line in Fig. 21 (a) displays the theoretical fit to the measured data when accounting for these factors. The effects of the three factors are evaluated quantitatively, as displayed in Figs 21 (b)-(d). The background light is the main source of the reduction of the photon bunching. We note that the strong attenuation in transmission to the value of $(1 - \beta)^2 \approx 0.5\%$ results in a small signal to background ratio. Nevertheless, the observed $g^{(2)}(0) \approx 21$ is among the highest values of photon bunching reported from a single-emitter system [75–79].
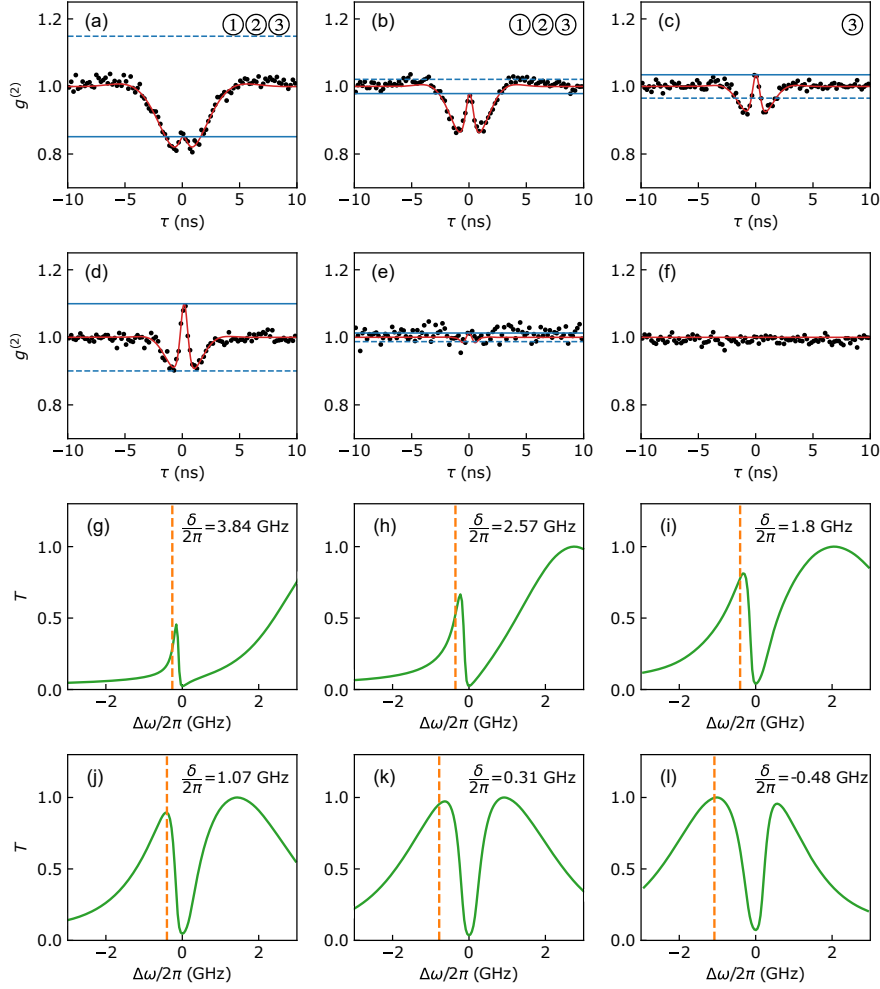
**Figure 22.** Photon statistics measured on the lower-frequency transmission peak at various cavity detunings. (a)-(f), Measured $g^{(2)}$-functions (black dots) and theoretical fits (red solid lines) at cavity detunings illustrated by the transmission spectra in (g)-(l), respectively. The solid blue lines mark the levels of $g^{(2)}(0)$, while the dashed blue lines indicate the levels of $2-g^{(2)}(0)$. The numbers in the upper right corner of each plot show the inequalities (see Eqs. 70-72) violated. (g)-(l), Transmission spectra (green curves) and laser frequencies (dashed orange lines) for the measurements in (a)-(f). The cavity detuning for each measurement is displayed in the upper right corner.

### 7.3. Detuned transmission: non-classical intensity fluctuations

In the next step, we explore the variations in photon statistics at different cavity and laser frequency detunings. The black dots in Fig. 22 (a)-(f) display the measured intensity-correlation functions on the lower-frequency transmission peak when the cavity resonance is tuned from the blue to the red side of the molecule. The corresponding transmission spectra are shown in (g)-(l). In (a)-(e), the intensity-correlation functions appear 'W'-shaped, with the value of $g^{(2)}(0)$ changing from 0.85 to 1.1 and then back to 1. The width of the 'W'-shaped feature decreases as the cavity is tuned closer to the molecule. In section 4, it was shown that the intracavity field $a$ can be expressed as the sum of

the driving field $E$ and the scattered field from the molecule $g\sigma_-$. The former is a coherent state following Poissonian statistics and the latter takes the properties of the resonant scattering by a single atom, which is antibunched. At large molecule-cavity detunings, the main contribution to the lower-frequency transmission peak is from the molecular scattering. The signal thus appears antibunched (see (a), (b)). When the cavity is tuned to the blue side of the molecule, the lower-frequency transmission peak changes from 'molecule'-like to 'cavity'-like. The intracavity field is then mainly from the driving field $E$, which follows Poissonian statistics (see (f)). The reduction in the feature width from (a) to (d) is a result of the Purcell effect, i.e. the lifetime of the molecule is reduced as the cavity is tuned closer to the molecule. The oscillatory behavior

around zero time delay is a result of the wavefunction collapse when a photon leaves the cavity, which results in a sudden change in the amplitude of the intracavity field [43].

One can classify the intensity fluctuation of the measured field as classical or nonclassical. In Ref. [42], a set of three inequalities were summarized to bound the intensity fluctuation of a classical field:

$$g^{(2)}(0) \geq 1 \,, \tag{70}$$

$$g^{(2)}(\tau) \leq g^{(2)}(0) \,, \tag{71}$$

$$|g^{(2)}(\tau) - 1| \leq |g^{(2)}(0) - 1| \,. \tag{72}$$

All three inequalities can be derived from the Cauchy-Schwarz inequality [42]. The first inequality shows that a classical light field cannot show antibunching, i.e. the intensity fluctuation of a classical field is bounded by the shot noise [80]. The second inequality shows that the $g^{(2)}$-function of a classical field cannot exceed its value at zero time delay. The third is derived by decomposing the intensity into its mean value and fluctuations, implying that the maximal deviation of the $g^{(2)}$-function from 1 appears at zero time delay. A violation of one of the three inequalities indicates that the field under study is nonclassical.

The solid blue lines in Fig. 22 (a)-(e) mark the levels of $g^{(2)}(0)$ in each of the plots, while the dashed blue lines show the levels of $2 - g^{(2)}(0)$. The areas in between the two lines are within the bound of Eq. 72. The numbers listed in the upper right corners of (a)-(f) indicate the inequalities violated in each data set. For larger cavity detunings, all three inequalities are violated. In this regime, the field is nonclassical since the main contribution comes from the scattering of the molecule. As the cavity detuning decreases, the field turns more 'cavity'-like and the $g^{(2)}$-functions fall within the bounds of all three inequalities. At an intermediate detuning (see (c)), the signal peaks and shows slight bunching at zero time delay, but the third inequality is still violated since the antibunching exceeds the bounds set by the blue lines.

The observed intensity-correlation functions reveal the rich temporal dynamics in the molecule-cavity system. In contrast to the structural effects such as spectral modifications which can be modeled classically [44, 45], the dynamic effects lead to nonclassical photon correlations, which is a result of pure quantum mechanical phenomena [43].

## 8. Interlinking two molecules with photons

Connecting individual atom-like quantum systems via flying photons is an enabling technique for the
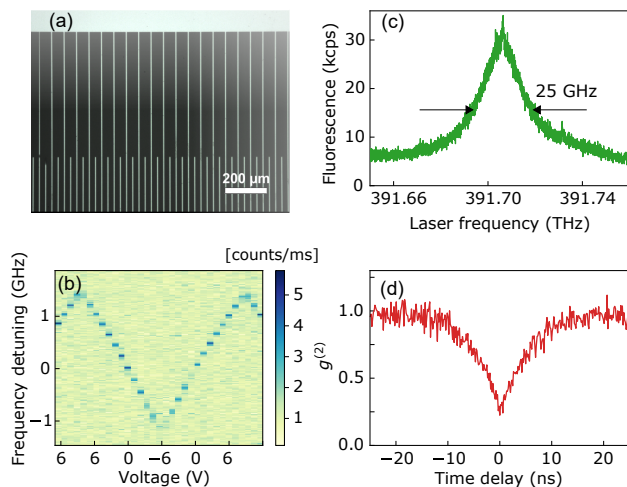


**Figure 23.** (a), Optical microscope image of the interdigitated ITO electrodes fabricated on a fused silica substrate. The spacing between an electrode and its neighboring counter-electrode (lower part) is 15 $\mu$m. (b), Frequency tuning of the source-molecule. The horizontal axis shows the applied voltage in a triangular waveform. The vertical axis denotes the detuning of the laser frequency with respect to the target-molecule. The color scale indicates the fluorescence count rates on the detector. (c), Fluorescence excitation spectrum to a $|e, v \neq 0\rangle$ level of the source-molecule. (d), Intensity autocorrelation measurement on the emitted 00ZPL photons.

future quantum internet [3]. In the past decade, exciting advances have been made in realizing photon-atom, photon-photon quantum gates [10, 79, 81] and elementary quantum networks [82]. Here, we demonstrate a further step towards this goal by connecting two single molecules with single photons.

We use the methods described in Ref. [83] to generate frequency-tunable single photons from a 'source'-molecule. First, a DBT-doped Ac crystal is prepared and transferred onto a fused-silica substrate. On the substrate, Indium-Tin-Oxide (ITO) electrodes are fabricated and patterned in an inter-digitated fashion, as displayed in Fig. 23 (a). The spacing between an electrode and its neighboring counter-electrode is 15 $\mu$m. The sample is then cooled to 1.4 K in a second cryostat located in a neighboring lab. We first identify a suitable source-molecule through fluorescence spectroscopy and microscopy. Using the DC Stark effect, we are able to tune the 00ZPL transition frequency of the source-molecule by applying a voltage to the electrodes. The effect of frequency tuning is displayed in Fig. 23 (b), where the molecule is tuned by 0.17 GHz/V in the frequency range (-1.2, 1.2) GHz with respect to the target-molecule. The linewidth of the 00ZPL transition is 41 MHz.

The source molecule is then excited to a higher vibronic level of its electronic excited state ($|e, v \neq 0\rangle$) using a Ti:sapphire laser. Its fluorescence emission is collected

by an aspheric lens. A narrow bandpass-filter is used to select the emission at the 00ZPL. Figure 23 (c) displays the fluorescence excitation spectrum to the vibronic level. About 30 000 photons per second are detected at the local optical table. An intensity autocorrelation measurement is performed on the 00ZPL emission, as displayed in Fig. 23 (d). An antibunching at zero time delay with $g^{(2)}(0) = 0.25$ confirms the purity of the single photons.

The single photons are then coupled into a single-mode fiber and guided to the microcavity experiment. There, the photons are coupled out of the fiber and sent through a half-wave plate which aligns their polarization to the cavity mode. They are focused by the aspheric lens and coupled into the cavity. The reflected photons are collimated by the same aspheric lens and detected by an APD.

The red dots in Fig. 24 (a) display the reflection spectrum of single-photons from the target-molecule. A peak in reflection with a width of about 600 MHz is observed as a result of the coherent interaction of the single-photons with the target-molecule. Although the signal-to-noise ratio is lower, the observed signal shows the same trend as that presented in Fig. 14 (c). To calibrate the signal, we detune the cavity resonance to lower frequency by about 5.5 GHz. The black dots in the same plot show the intensity of the single-photons reflected from the detuned cavity. Here, a notable dip appears at a slightly blue-shifted frequency with respect to the target-molecule. The small dip stems from destructive interference of the molecular scattering and the cavity field. At this detuning, a small Purcell factor ($F = 3.3$) is still present, thus the photons scattered by the target-molecule are captured with a high efficiency by the cavity mode and give rise to the reflection dip. The slight blue shift of the dip results from the cavity-modified Lamb shift. A quantitative description is given by the theoretical fits shown by the solid lines.

To further verify the observations in Fig. 24 (a), we repeat the measurements using a weak laser beam. Figure 24 (b) presents the reflection spectra from the resonantly coupled (red) and cavity-detuned (black) systems measured with a weak laser beam, showing the same features as in (a). We note that the depth and width of the dip in the detuned spectrum differs from that measured by the single photons. The deviations originate from the linewidth difference of the single photons (41 MHz) and the laser beam ($< 1$ MHz).

This experiment demonstrates the feasibility of interlinking two single molecules using single photons. The coupling strength between the two molecules can be improved by placing the source-molecule
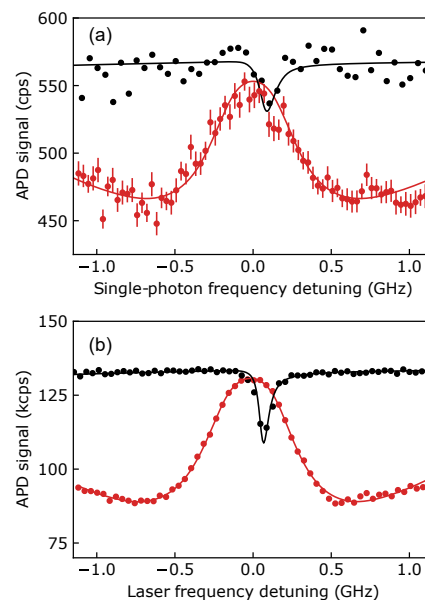


**Figure 24.** (a), Intensity of single-photons reflected from the molecule-cavity system as a function of their frequency detuning. The red dots present the reflection spectrum from the resonantly-coupled molecule-cavity system. The black dots present the reflection spectrum when the cavity is detuned by 5.5 GHz from the target-molecule. The error bars indicate the shot noise. The solid lines show the theoretical fits considering a weak laser beam with a linewidth of 41 MHz. (b), The same as in (a) but measured with a weak laser beam.

in a microcavity as well. This experiment also opens new doors for performing nonlinear optical experiments with 'true' single photons. To this end, the source molecule can be excited using a pulsed laser. The periodically spaced single-photons can then be converted to multi-photon pulses via temporal multiplexing [84]. Exciting experiments such as single-photon pump-probe on a single molecule can be within reach.

## 9. Conclusion and outlook

In this tutorial, we presented a series of studies on efficient light-molecule coupling enabled by a Fabry-Perot microcavity. Resonant coupling to the cavity resonance enhances the 00ZPL transition of a single molecule by a factor of $\sim 40$, thus converting it to a nearly ideal two-level system. The strong radiative enhancement also led to an efficient coupling of the molecular emission to the cavity mode. This enabled the observation of several unprecedented linear and nonlinear optical effects in molecular systems, such as 99% extinction of the cavity transmission, $\pm 66°$ phase shift of a laser beam as well as saturation with less than half a photon per lifetime. We confirmed the strong optical nonlinearity of the system and observed rich

non-Poissonian photon statistics within. Furthermore, we showed that two molecules can be coupled via single photons. These observations opened the door to realizing linear and nonlinear quantum photonic circuits based on organic platforms.

The use of a microcavity allowed us to accelerate an optical transition from the megahertz to the gigahertz range without reaching the strong coupling regime, such that the emission process is greatly enhanced but not limited by the bandwidth of the cavity. This regime is optimal for achieving fast information and energy extraction from the material qubits [85–87]. Although the experiments presented in this tutorial are based on PAH molecules, the principle of cavity enhancement is not limited to organic systems. In recent years, many efforts have been invested in searching for material systems with suitable level structures to facilitate a quantum interface between light and matter. Systems such as neutral atoms [81, 82, 88, 89] and ions [90–92] in the gas phase and quantum dots [93, 94], color centers [77, 95, 96] and rare-earth ions [97–100] in the solid state are promising candidates for this purpose. Integrating these emitters with open-access Fabry-Perot microcavities [60, 101–111] to boost light-matter coupling is an emerging field of research.

There are several exciting prospects which can be explored on the established molecule-cavity system. First, by using a bright and pulsed single photon source and active temporal multiplexing [84], one can time the arrival of multiple photons at the molecule. The single-photon source can be realized by using a cryogenically compatible antenna structure [112] or by placing a second molecule in another microcavity. The system is then capable for demonstrating photon-photon interactions mediated by a single molecule, i.e. a single-photon 'pump-probe' experiment. Second, by structuring electrodes on the planar mirror, the resonance frequencies of single molecules in the cavity mode can be tuned with respect to each other. This will allow controlled studies of the interaction between two or more molecules mediated by photons in the cavity [113, 114]. Cooperative effects such as coherent dipole-dipole coupling [115], polaritonic states and light localization [116, 117] can be explored. Last but not least, the open and low-volume microcavity also allows sensing and imaging of nanoparticles [56, 118]. Combination of microcavities with micro-fluidic systems is promising for realizing on-chip chemical- and bio-sensors [119, 120].

## Acknowledgement

## References

[1] Jaeger L 2019 *The Second Quantum Revolution: From Entanglement to Quantum Computing and Other Super-Technologies* (Springer International Publishing)

[2] Acín A, Bloch I, Buhrman H, Calarco T, Eichler C, Eisert J, Esteve D, Gisin N, Glaser S J and et al F J 2018 *New Journal of Physics* **20** 080201

[3] Kimble H J 2008 *Nature* **453** 1023–1030

[4] Cirac J I, Zoller P, Kimble H J and Mabuchi H 1997 *Phys. Rev. Lett.* **78** 3221–3224

[5] Stobińska M, Alber G and Leuchs G 2009 *Europhys. Lett.* **86** 14007

[6] Leuchs G and Sondermann M 2012 *Physica Scripta* **85** 058101

[7] Zumofen G, Mojarad N M, Sandoghdar V and Agio M 2008 *Physical Review Letters* **101**

[8] Chang D E, Vuletić V and Lukin M D 2014 *Nat. Photon.* **8** 685–694

[9] Maser A, Gmeiner B, Utikal T, Götzinger S and Sandoghdar V 2016 *Nat. Photon.* **10** 450–453

[10] Hacker B, Welte S, Rempe G and Ritter S 2016 *Nature* **536** 193–196

[11] Moerner W, Orrit M, Wild U and Basché T (eds) 1996 *Single-Molecule Optical Detection, Imaging and Spectroscopy* (Wiley)

[12] Lounis B and Orrit M 2005 *Rep. Prog. Phys.* **68** 1129–1179

[13] Aharonovich I, Englund D and Toth M 2016 *Nat. Photon.* **10** 631–641

[14] Vahala K J 2003 *Nature* **424** 839–846

[15] Purcell E M 1946 *Phys. Rev.* **69** 674–674

[16] Wang D, Kelkar H, Martin-Cano D, Rattenbacher D, Shkarin A, Utikal T, Götzinger S and Sandoghdar V 2019 *Nature Physics* **15** 483–489

[17] Wang D 2019 *Coherent Coupling of a Single Molecule to a Fabry-Perot Microcavity* Doctoral Thesis Friedrich-Alexander-Universität Erlangen-Nürnberg

[18] Klessinger M and Michl J 1995 *Excited states and photochemistry of organic molecules* (Wiley-VCH)

[19] Moerner W E and Kador L 1989 *Phys. Rev. Lett.* **62** 2535–2538

[20] Kasha M 1950 *Discuss. Faraday Soc.* **9** 14–19

[21] Franck J and Dymond E G 1926 *Trans. Faraday Soc.* **21** 536–542

[22] Condon E 1926 *Phys. Rev.* **28** 1182–1201

[23] Nicolet A A L, Bordat P, Hofmann C, Kol'chenko M A, Kozankiewicz B, Brown R and Orrit M 2007 *ChemPhysChem* **8** 1929–1936

[24] Einstein A 1916 *Verhandlungen der Deutsche Physikalische Gesellschaft* **18** 318–323

[25] Loudon R 2000 *The Quantum Theory of Light* (Oxford University Press)

[26] Walther H, Varcoe B T H, Englert B G and Becker T 2006 *Rep. Prog. Phys.* **69** 1325–1382

[27] Haroche S and Raimond J 2006 *Exploring the Quantum: Atoms, Cavities, and Photons* (Oxford University Press)

[28] Fox M 2006 *Quantum Optics: An Introduction* (Oxford University Press)

[29] Milonni P W 1994 *The Quantum Vacuum: An Introduction to Quantum Electrodynamics* (Academic Press)

[30] Sauvan C, Hugonin J P, Maksymov I S and Lalanne P 2013 *Phys. Rev. Lett.* **110** 237401

[31] Petermann K 1979 *IEEE J. Quantum Electron.* **15** 566–570

[32] Khitrova G, Gibbs H M, Kira M, Koch S W and Scherer A 2006 *Nat. Phys.* **2** 81–90

[33] Choi Y, Kang S, Lim S, Kim W, Kim J R, Lee J H and An K 2010 *Phys. Rev. Lett.* **104** 153601

[34] Berman P R (ed) 1994 *Cavity quantum electrodynamics* (Academic Press)

[35] Auffèves-Garnier A, Simon C, Gérard J M and Poizat J P 2007 *Phys. Rev. A* **75** 053823

[36] Nicolet A A L, Hofmann C, Kol'chenko M A, Kozankiewicz B and Orrit M 2007 *ChemPhysChem* **8** 1215–1220

[37] Fano U 1961 *Phys. Rev.* **124**(6) 1866–1878

[38] Heinzen D J and Feld M S 1987 *Phys. Rev. Lett.* **59**(23) 2623–2626

[39] Lamb W E and Retherford R C 1947 *Phys. Rev.* **72** 241–243

[40] Reiserer A, Ritter S and Rempe G 2013 *Science* **342** 1349–1351

[41] Carmichael H J 1985 *Phys. Rev. Lett.* **55** 2790–2793

[42] Rice P R and Carmichael H J 1988 *IEEE J. Quantum Electron.* **24** 1351–1366

[43] Carmichael H J and Rice P R 1991 *Opt. Commun.* **82** 73–79

[44] Zhu Y, Gauthier D J, Morin S E, Wu Q, Carmichael H J and Mossberg T W 1990 *Phys. Rev. Lett.* **64**(21) 2499–2502

[45] Tanji-Suzuki H, Leroux I D, Schleier-Smith M H, Cetina M, Grier A T, Simon J and Vuletić V 2011 Interaction between Atomic Ensembles and Optical Resonators: Classical Description *Advances in Atomic, Molecular, and Optical Physics* vol 60 (Academic Press) pp 201 – 237

[46] Kimble H J 1998 *Phys. Scr.* **T76** 127–137

[47] Raimond J M, Brune M and Haroche S 2001 *Rev. Mod. Phys.* **73** 565–582

[48] Thompson R J, Rempe G and Kimble H J 1992 *Phys. Rev. Lett.* **68**(8) 1132–1135

[49] Rempe G, Thompson R J, Kimble H J and Lalezari R 1992 *Opt. Lett.* **17** 363–365

[50] Hood C J, Kimble H J and Ye J 2001 *Phys. Rev. A* **64**(3) 033804

[51] Steinmetz T, Colombe Y, Hunger D, Hänsch T W, Balocchi A, Warburton R J and Reichel J 2006 *Appl. Phys. Lett.* **89** 111110

[52] Hunger D, Steinmetz T, Colombe Y, Deutsch C, Hänsch T W and Reichel J 2010 *New J. Phys.* **12** 065038

[53] Hunger D, Deutsch C, Barbour R J, Warburton R J and Reichel J 2012 *AIP Advances* **2** 012119

[54] Toninelli C, Delley Y, Stöferle T, Renn A, Götzinger S and Sandoghdar V 2010 *Appl. Phys. Lett.* **97** 021107

[55] Dolan P R, Hughes G M, Grazioso F, Patton B R and Smith J M 2010 *Opt. Lett.* **35** 3556–3558

[56] Kelkar H, Wang D, Martín-Cano D, Hoffmann B, Christiansen S, Götzinger S and Sandoghdar V 2015 *Phys. Rev. Applied* **4** 054010

[57] Muller A, Flagg E B, Lawall J R and Solomon G S 2010 *Opt. Lett.* **35** 2293–2295

[58] Orloff J, Swanson L and Utlaut M 2003 *High Resolution Focused Ion Beams: FIB and its Applications* (Springer US)

[59] Trichet A A P, Dolan P R, Coles D M, Hughes G M and Smith J M 2015 *Opt. Express* **23** 17205–17216

[60] Albrecht R, Bommer A, Pauly C, Mücklich F, Schell A W, Engel P, Schröder T, Benson O, Reichel J and Becher C 2014 *Appl. Phys. Lett.* **105** 073113

[61] Schwoerer M and Wolf H C 2008 *Purification of Materials, Crystal Growth and Preparation of Thin Films* (Wiley-VCH)

[62] Wang D, Kelkar H, Martin-Cano D, Utikal T, Götzinger S and Sandoghdar V 2017 *Phys. Rev. X* **7** 021014

[63] Trebbia J B, Ruf H, Tamarat P and Lounis B 2009 *Opt. Express* **17** 23986–23991

[64] Pazzagli S, Lombardi P, Martella D, Colautti M, Tiribilli B, Cataliotti F S and Toninelli C 2018 *ACS Nano* **12** 4295–4303

[65] Wrigge G, Gerhardt I, Hwang J, Zumofen G and Sandoghdar V 2008 *Nat. Phys.* **4** 60–66

[66] Scully M and Zubairy M 1997 *Quantum Optics* (Cambridge University Press)

[67] Pototschnig M, Chassagneux Y, Hwang J, Zumofen G, Renn A and Sandoghdar V 2011 *Phys. Rev. Lett.* **107** 063001

[68] Becker W 2015 *Advanced Time-Correlated Single Photon Counting Applications* Springer Series in Chemical Physics (Springer International Publishing)

[69] Boyd R W 2008 *Nonlinear Optics* (Academic Press)

[70] Bonato C, Haupt F, Oemrawsingh S S R, Gudat J, Ding D, van Exter M P and Bouwmeester D 2010 *Phys. Rev. Lett.* **104**(16) 160503

[71] Witthaut D, Lukin M D and Sørensen A S 2012 *Europhys. Lett.* **97** 50007

[72] Ralph T C, Söllner I, Mahmoodian S, White A G and Lodahl P 2015 *Phys. Rev. Lett.* **114**(17) 173603

[73] Shen J T and Fan S 2007 *Phys. Rev. Lett.* **98**(15) 153003

[74] Brown R H and Twiss R Q 1956 *Nature* **177** 27–29

[75] Snijders H, Frey J A, Norman J, Bakker M P, Langman E C, Gossard A, Bowers J E, van Exter M P, Bouwmeester D and Löffler W 2016 *Nat. Commun.* **7** 12578

[76] Bennett A J, Lee J P, Ellis D J P, Farrer I, Ritchie D A and Shields A J 2016 *Nat. Nanotech.* **11** 857–860

[77] Sipahigil A, Evans R E, Sukachev D D, Burek M J, Borregaard J, Bhaskar M K, Nguyen C T, Pacheco J L, Atikian H A, Meuwly C and et al 2016 *Science* **354** 847–850

[78] Javadi A, Söllner I, Arcari M, Hansen S L, Midolo L, Mahmoodian S, Kiršanskė G, Pregnolato T, Lee E H, Song J D and et al 2015 *Nat. Commun.* **6** 8655

[79] Tiecke T G, Thompson J D, de Leon N P, Liu L R, Vuletić V and Lukin M D 2014 *Nature* **508** 241–244

[80] Paul H 1982 *Rev. Mod. Phys.* **54**(4) 1061–1102

[81] Reiserer A and Rempe G 2015 *Rev. Mod. Phys.* **87** 1379–1418

[82] Ritter S, Nölleke C, Hahn C, Reiserer A, Neuzner A, Uphoff M, Mücke M, Figueroa E, Bochmann J and Rempe G 2012 *Nature* **484** 195–200

[83] Rezus Y L A, Walt S G, Lettow R, Renn A, Zumofen G, Götzinger S and Sandoghdar V 2012 *Phys. Rev. Lett.* **108** 093601

[84] Wang H, He Y, Li Y H, Su Z E, Li B, Huang H L, Ding X, Chen M C, Liu C, Qin J and et al 2017 *Nat. Photon.* **11** 361–365

[85] Madsen K H, Ates S, Liu J, Javadi A, Albrecht S M, Yeo I, Stobbe S and Lodahl P 2014 *Phys. Rev. B* **90**(15) 155303

[86] Grange T, Hornecker G, Hunger D, Poizat J P, Gérard J M, Senellart P and Auffèves A 2015 *Phys. Rev. Lett.* **114**(19) 193601

[87] Somaschi N, Giesz V, De Santis L, Loredo J C, Almeida M P, Hornecker G, Portalupi S L, Grange T, Antón C, Demory J and et al 2016 *Nat. Photon.* **10** 340–345

[88] Volz J, Weber M, Schlenk D, Rosenfeld W, Vrana J, Saucke K, Kurtsiefer C and Weinfurter H 2006 *Phys. Rev. Lett.* **96** 030404

[89] Wilk T, Webster S C, Kuhn A and Rempe G 2007 *Science* **317** 488–490

[90] Blinov B B, Moehring D L, Duan L M and Monroe C 2004 *Nature* **428** 153–157

[91] Duan L M and Monroe C 2010 *Rev. Mod. Phys.* **82** 1209–1224

[92] Stute A, Casabone B, Brandstätter B, Friebe K, Northup T E and Blatt R 2013 *Nat. Photon.* **7** 219–222

[93] Gao W B, Fallahi P, Togan E, Miguel-Sanchez J and Imamoglu A 2012 *Nature* **491** 426–430

[94] Delley Y L, Kroner M, Faelt S, Wegscheider W and İmamoğlu A 2017 *Phys. Rev. B* **96** 241410(R)

[95] Togan E, Chu Y, Trifonov A S, Jiang L, Maze J, Childress L, Dutt M V G, Sørensen A S, Hemmer P R, Zibrov A S and et al 2010 *Nature* **466** 730–734

[96] Bernien H, Hensen B, Pfaff W, Koolstra G, Blok M S, Robledo L, Taminiau T H, Markham M, Twitchen D J, Childress L and et al 2013 *Nature* **497** 86–90

[97] Kolesov R, Xia K, Reuter R, Stöhr R, Zappe A, Meijer J, Hemmer P and Wrachtrup J 2012 *Nat. Commun.* **3** 1029

[98] Utikal T, Eichhammer E, Petersen L, Renn A, Götzinger S and Sandoghdar V 2014 *Nat. Commun.* **5** 3627

[99] Zhong M, Hedges M P, Ahlefeldt R L, Bartholomew J G, Beavan S E, Wittig S M, Longdell J J and Sellars M J 2015 *Nature* **517** 177–180

[100] Dibos A M, Raha M, Phenicie C M and Thompson J D 2018 *Phys. Rev. Lett.* **120** 243601

[101] Muller A, Flagg E B, Metcalfe M, Lawall J and Solomon G S 2009 *Appl. Phys. Lett.* **95** 173101

[102] Miguel-Sánchez J, Reinhard A, Togan E, Volz T, Imamoglu A, Besga B, Reichel J and Estève J 2013 *New J. Phys.* **15** 045002

[103] Greuter L, Starosielec S, Kuhlmann A V and Warburton R J 2015 *Phys. Rev. B* **92** 045302

[104] Najer D, Söllner I, Sekatski P, Dolique V, Löbl M C, Riedel D, Schott R, Starosielec S, Valentin S R, Wieck A D, Sangouard N, Ludwig A and Warburton R J 2019 *Nature* **575** 622–627

[105] Johnson S, Dolan P R, Grange T, Trichet A A P, Hornecker G, Chen Y C, Weng L, Hughes G M, Watt A A R, Auffèves A and Smith J M 2015 *New J. Phys.* **17** 122003

[106] Kaupp H, Hümmer T, Mader M, Schlederer B, Benedikter J, Haeusser P, Chang H C, Fedder H, Hänsch T W and Hunger D 2016 *Phys. Rev. Applied* **6** 054010

[107] Benedikter J, Kaupp H, Hümmer T, Liang Y, Bommer A, Becher C, Krueger A, Smith J M, Hänsch T W and Hunger D 2017 *Phys. Rev. Applied* **7** 024031

[108] Bogdanović S, Liddy M S Z, van Dam S B, Coenen L C, Fink T, Lončar M and Hanson R 2017 *APL Photonics* **2** 126101

[109] Riedel D, Söllner I, Shields B J, Starosielec S, Appel P, Neu E, Maletinsky P and Warburton R J 2017 *Phys. Rev. X* **7**(3) 031040

[110] Casabone B, Benedikter J, Hümmer T, Oehl F, de Oliveira Lima K, Hänsch T W, Ferrier A, Goldner P, de Riedmatten H and Hunger D 2018 *New J. Phys.* **20** 095006

[111] Merkel B, Ulanowski A and Reiserer A 2020 *Phys. Rev. X* **10**(4) 041025

[112] Chen X W, Götzinger S and Sandoghdar V 2011 *Opt. Lett.* **36** 3545–3547

[113] van Loo A F, Fedorov A, Lalumière K, Sanders B C, Blais A and Wallraff A 2013 *Science* **342** 1494–1496

[114] Evans R E, Bhaskar M K, Sukachev D D, Nguyen C T, Sipahigil A, Burek M J, Machielse B, Zhang G H, Zibrov A S, Bielejec E, Park H, Lončar M and Lukin M D 2018 *Science* **362** 662–665

[115] Hettich C, Schmitt C, Zitzmann J, Kühn S, Gerhardt I and Sandoghdar V 2002 *Science* **298** 385–389

[116] Diniz I, Portolan S, Ferreira R, Gérard J M, Bertet P and Auffèves A 2011 *Phys. Rev. A* **84** 063810

[117] Haakh H R, Faez S and Sandoghdar V 2016 *Phys. Rev. A* **94** 053840

[118] Mader M, Reichel J, Hänsch T W and Hunger D 2015 *Nat. Commun.* **6** 7249

[119] Trichet A A P, Dolan P R, James D, Hughes G M, Vallance C and Smith J M 2016 *Nano Letters* **16** 6172–6177 publisher: American Chemical Society

[120] Vallance C, Trichet A A P, James D, Dolan P R and Smith J M 2016 *Nanotechnology* **27** 274003